Appendix A

Monte Carlo Simulation of Single- and Multi-Photon Events

A theoretical description of the reaction $e^+e^- \to \nu\bar{\nu}\gamma(\gamma)$ was given in Chapter 2. In this appendix I describe in detail the algorithms used to simulate the higher-order QED corrections and give a formula for the differential cross section for the $\mathcal{O}(\alpha)$ process $e^+e^- \to \nu\bar{\nu}\gamma$.

A.1 The Reaction $e^+e^- \to \nu\bar{\nu}\gamma$ at Tree Level

In order to achieve an accurate simulation of the single- and multi-photon production at LEP, one needs to know the exact cross sections of the reactions $e^+e^- \to \nu\bar{\nu}\gamma$ and $e^+e^- \to \nu\bar{\nu}\gamma\gamma$ which correspond to the tree-level (*bare*) single- and double-photon emissions. Neglecting the electron mass and photon radiation from the W boson propagator in the t–channel,[1] the differential cross section of the bare single-photon emission,

$$e^+ (p_+) + e^- (p_-) \longrightarrow \bar{\nu} (q_+) + \nu (q_-) + \gamma (k), \qquad (A.1)$$

was calculated analytically in Reference [233] and is given by

$$\frac{d\sigma}{d\cos\theta_\gamma\, dE_\gamma} = \frac{G_F^2\, \alpha}{6\pi^2} \frac{s'}{s^2 E_\gamma \sin^2\theta_\gamma} \left[(s - \kappa_+)^2 F(\eta_+) + (s - \kappa_-)^2 F(\eta_-) \right], \qquad (A.2)$$

---

[1] At LEP2 energies, $\sqrt{s} \simeq 200$ GeV, photon emission from the W boson in the t–channel adds only about 0.5% to the total cross section of this process [18]. As shown in Figure 2.6e, this diagram contains two W propagators and, thus, is suppressed by an additional factor of $1/M_W^2$. However, it should be noted that photon radiation from the W propagator is included in the calculation of the exact matrix elements used in the KKMC [17] and NUNUGPV [27] MC event generators.

with

$$\eta_\pm = \frac{s - \kappa_\pm}{M_W^2} \,, \tag{A.3}$$

$$F(\eta_\pm) = N_\nu \left(g_L^2 + g_R^2\right) \frac{M_Z^4}{|Z|^2} + 3g_L \frac{M_Z^2 \operatorname{Re} Z}{|Z|^2} \frac{1}{\eta_\pm} \left[3 + \frac{2}{\eta_\pm} - 2\left(1 + \frac{1}{\eta_\pm}\right)^2 \ln\left(1 + \eta_\pm\right)\right]$$

$$+ \frac{3}{\eta_\pm^2} \left[\left(1 + \eta_\pm\right)\left(1 - \frac{2}{\eta_\pm} \ln\left(1 + \eta_\pm\right)\right) + 1\right] \,, \tag{A.4}$$

where E_γ and θ_γ are the energy and the polar angle of the emitted photon, N_ν denotes the number of neutrinos species, $g_R = \sin^2 \theta_W$, and $g_L = -\frac{1}{2} + \sin^2 \theta_W$. The following notation is used in the above equations:

$$
\begin{aligned}
s &= \left(p_+ + p_-\right)^2 , \\
s' &= \left(q_+ + q_-\right)^2 , \\
\kappa_\pm &= 2p_\pm k = 2E_e E_\gamma \left(1 \pm \cos\theta_\gamma\right) , \\
Z &= s' - M_Z^2 + iM_Z\Gamma_Z .
\end{aligned}
\tag{A.5}
$$

The three terms of Equation A.4 are identified easily within the Feynman calculus: the first one describes the two s–channel Z exchange diagrams (Figure 2.6a,b), the last term corresponds to the two t–channel W exchange diagrams (Figure 2.6c,d), and the middle term accounts for the interference between the s– and t–channel diagrams.

At low photon energies and polar angles, the differential cross section given by Equation A.2 behaves[2] as $\sim 1/(E_\gamma \sin^2 \theta_\gamma)$. Therefore, the cross section of this process is divergent at tree level when the photon becomes soft, $E_\gamma \to 0$ (*infrared divergence*), or when the electron (positron) and the emitted photon become collinear, $\sin\theta_\gamma \to 0$. The collinear divergence can be eliminated if we take account the nonzero electron mass, whereas the infrared divergence can be canceled by including the $\mathcal{O}(\alpha)$ diagrams containing virtual photon loops [234].

---

[2]It should be noted that, as expected, this expression has the same singularities as the radiator function defined in Section 2.2.2.

A.2 Structure Function Techniques

In e^+e^- collisions, the large QED corrections introduced by the undetected initial state radiation (soft and/or collinear photon emission) can be successfully described within the framework of the QED *structure functions* [235]. In this formalism, the incoming electron (positron) is assumed to consist of a "cloud" of virtual electrons and photons, and the emitted photons are assumed to be almost collinear with the incoming electron. To include effects of the ISR, the total cross section of a given process $e^+e^- \to X$ can then be calculated as

$$\sigma_{ISR}(s) = \int dx_1\, dx_2\; D(x_1, s) D(x_2, s)\, \sigma_0(x_1 x_2 s)\,, \qquad (A.6)$$

where $\sigma_0(s)$ is the non-radiative cross section as a function of center-of-mass energy squared (s) and $D(x, s)$ is the structure of the incoming electron (positron), defined as the probability that, after the initial state radiation, the electron energy is equal to $x\sqrt{s}/2$.

The $\mathcal{O}(\alpha^2)$ structure function $D(x, s)$ can be obtained by solving the Lipatov–Altarelli–Parisi evolution equation and is given by [236]

$$
\begin{aligned}
D(x, s) \;=\;& \frac{\exp\left\{\frac{1}{2}\beta\left(\frac{3}{4} - \gamma_E\right)\right\}}{\Gamma\left(1 + \frac{1}{2}\beta\right)} \frac{\beta}{2}(1 - x)^{\frac{\beta}{2} - 1} - \frac{\beta}{4}(1 + x) \\
&+ \frac{1}{32}\beta^2\left[-4(1 + x)\ln(1 - x) + 3(1 + x)\ln x - 4\frac{\ln x}{1 - x} - 5 - x\right],
\end{aligned} \qquad (A.7)
$$

where $\beta = 2\frac{\alpha}{\pi}(L - 1)$, $L = \ln\left(s/m_e^2\right)$ is the collinear logarithm, γ_E is the Euler constant, and $\Gamma(z)$ is the gamma function. The first exponentiated Gribov–Lipatov term describes multi-photon soft emission, and the second and third terms come from the single and double hard collinear bremsstrahlung processes, respectively [21, 237].

This formalism is simple and intuitive, and it was shown that for e^+e^- processes at LEP2 energies this procedure can provide a precision of up to 0.1% [238]. However, since the structure functions are derived by integrating over all photon energies and polar angles, this approach is limited to situations in which only the ISR-corrected

cross section is of interest. Additional phase space cuts are difficult to implement. Specific photonic observables (for instance the fraction of photons above a given energy or angular threshold) are impossible to extract.

In order to address this problem, the authors of the NUNUGPV Monte Carlo program [27] have introduced a corrected structure function $\tilde{D}(x, \cos\theta_\gamma; s)$ which is suitable for simulating the emission of ISR photons with finite, detectable transverse momentum:

$$\tilde{D}(x, \cos\theta_\gamma; s) = D(x; s)\, f(\cos\theta_\gamma; s)\,, \tag{A.8}$$

where the angular function $f(\cos\theta_\gamma; s)$ was chosen to reproduce the leading order behavior of $1/(p_e \cdot k_\gamma)$ and $D(x; s)$ is the collinear structure function, as given by Equation A.8. The higher-order QED corrections are then included in the total cross section of the reaction $e^+e^- \to \nu\bar{\nu}\gamma(\gamma)$ as

$$
\begin{aligned}
\sigma_{\nu\bar{\nu}\gamma(\gamma)} &= \int dx_1 dx_2 dc_\gamma^{(1)} dc_\gamma^{(2)}\, \tilde{D}(x_1, c_\gamma^{(1)}; s)\tilde{D}(x_2, c_\gamma^{(2)}; s)\, \Theta(cuts) \\
&\quad \times \left(\sigma_{1\gamma} + \sigma_{2\gamma} + \sigma_{3\gamma}\right)\,,
\end{aligned} \tag{A.9}
$$

where $c_\gamma \equiv \cos\theta_\gamma$; $\sigma_{1\gamma}, \sigma_{2\gamma}, \sigma_{3\gamma}$ denote the exact cross sections of the tree-level processes $e^+e^- \to \nu\bar{\nu}n\gamma$, $n = 1, 2$, and 3. The quantities $\sigma_{n\gamma}$ are evaluated for the photon energies and polar angles above a chosen set of cuts, $E_\gamma > E_{min}$ and $\sin\theta_\gamma > \sin\theta_{min}$. In Equation A.9, the function $\Theta(cuts)$ restricts the photons in $\tilde{D}(x, c_\gamma; s)$ to be below the thresholds E_{min} and θ_{min}, thus avoiding the overlap.

In a similar fashion, the QED corrected cross section of the reaction $e^+e^- \to \nu\bar{\nu}\,\gamma\gamma(\gamma)$ can be calculated as

$$
\begin{aligned}
\sigma_{\nu\bar{\nu}\gamma\gamma(\gamma)} &= \int dx_1 dx_2 dc_\gamma^{(1)} dc_\gamma^{(2)}\, \tilde{D}(x_1, c_\gamma^{(1)}; s)\tilde{D}(x_2, c_\gamma^{(2)}; s)\, \Theta(cuts) \\
&\quad \times \left(\sigma_{2\gamma} + \sigma_{3\gamma}\right)\,.
\end{aligned} \tag{A.10}
$$

A.3   The YFS Scheme

A general treatment of the infrared divergences occurring in QED was given by
D.R. Yennie, S.C. Frautschi, and H. Suura in their classic paper [239], which also
described a very powerful and accurate way of estimating radiative corrections to
high-energy processes known as the YFS scheme.

The idea behind the YFS scheme is to separate the phase space available for the
emission of real photons into two regions via a cut on the photon energy such that
photons are considered "infrared" if their energies are below $\varepsilon \cdot E_{beam}$. The parameter
ε can be set arbitrarily low, e.g., in the `KKMC` generator it is typically chosen to be
$\varepsilon = 10^{-5}$, so that this cut has no effect on the simulation of the real photon emission.
The contribution of the infrared photons can then be used to cancel the virtual
infrared divergences to all orders of α. After the cancellation, the real and virtual
infrared contributions can be summed into a universal YFS form factor [240]:

$$F^{\text{YFS}}(\varepsilon) \;\; = \;\; \exp\left[\frac{\alpha}{\pi} \left(\frac{1}{2} \ln \frac{s}{m_e{}^2} - 1 + \frac{\pi^2}{3} \right) + \frac{2\alpha}{\pi} \left(\ln \frac{s}{m_e{}^2} - 1 \right) \ln \varepsilon \right] . \quad \text{(A.11)}$$

The emission of the visible real photons can then be corrected to reproduce exact
results as given by the corresponding matrix elements. For example, for the reaction
$e^+(p_1)\, e^-(p_2) \to \nu(q_1)\, \bar{\nu}(q_2)$, the total cross section including an arbitrary number of
real and virtual photons can be calculated as

$$\begin{aligned}
\sigma \;\; = \;\; & F^{\text{YFS}}(\varepsilon) \int \frac{d^3\vec{q}_1}{q_1^0} \frac{d^3\vec{q}_2}{q_2^0} \sum_{n=0}^{\infty} \left\{ \frac{1}{n!} \left[\prod_{i=1}^{n} \frac{d^3\vec{k}_i}{k_i^0} \tilde{S}(p_1, p_2, k_i)\, \Theta\!\left(\frac{2k_i^0}{\sqrt{s}} - \varepsilon \right) \right] \times \right. \\
& \times\, \delta^4\left(p_1 + p_2 - q_1 - q_2 - \sum_{i=1}^{n} k_i \right) \times \\
& \left. \times \left(\beta_0 + \sum_{j=1}^{n} \frac{\beta_1(k_j)}{\tilde{S}(k_j)} + \sum_{j,l=1, j\neq l}^{n} \frac{\beta_2(k_j, k_l)}{\tilde{S}(k_j)\tilde{S}(k_l)} + \ldots \right) \right\} .
\end{aligned} \qquad \text{(A.12)}$$

The YFS form factor $F^{\text{YFS}}(\varepsilon)$ covers the contribution of factorizing infrared real
and virtual photons to all orders. The integral over the phase space of the final-
state particles consists of an integration over the two outgoing momenta, q_1 and q_2,

multiplied by a sum over all possible numbers of photons k_i with an energy above the "infrared" threshold εE_{beam}. The conservation of the four-momentum is enforced by the δ-function in the second line. The cross section of the reaction $e^+e^- \to \nu\bar{\nu}(\gamma)$ and higher-order corrections to the hard-photon radiation are included in the hard photon residuals β_i, e.g., β_0 is equal to the Born-level differential cross section $\sigma(e^+e^- \to \nu\bar{\nu})$ and β_1 includes the exact differential cross section of the reaction $e^+e^- \to \nu\bar{\nu}\gamma$ (see Section A.1). The function $\tilde{S}(k)$ denotes the universal factorizing "eikonal factor" of the real-photon radiation. For a pair of two external charged lines with four–momenta p_1 and p_2, it is given by

$$\tilde{S}(k) \;=\; \frac{\alpha}{4\pi} \left[\frac{p_2}{kp_2} - \frac{p_1}{kp_1} \right]^2 . \tag{A.13}$$

The YFS technique is applicable to arbitrary initial and final state particles. The number of photons that are explicitly produced is not constrained. The calculated cross section is independent of the parameter ε. In addition, contrary to the structure function formalism, any photon emission process can be corrected by the appropriate matrix elements to the chosen order of α, including interference effects for the multi-photon final states. Details of the actual implementation of the YFS scheme can be found in Reference [240].

The YFS technique has been used in many theoretical calculations and Monte Carlo generators. In this thesis, the reaction $e^+e^- \to \nu\bar{\nu}\gamma(\gamma)$ is simulated mainly with the KKMC generator [17], which employs a more advanced Coherent Exclusive Exponentiation (CEEX) method to simulate higher-order QED corrections [25]. The CEEX technique is based on the YFS scheme; however, the CEEX is formulated in terms of spin amplitudes, i.e., the higher-order effects are included before the spin summation.

Appendix B

RFQ System in Detail

The RFQ calibration system, method, and results were presented in Chapter 5. In this appendix I describe in detail the individual components of the RFQ system.

It should be noted that the design of the L3 RFQ calibration system was unique, as it was the only physics experiment requiring the use of such a highly energetic neutral particle beam (NPB). Interestingly enough, a very similar system was used as part of the development of NPB technology for strategic defense applications. *The Beam Experiments Aboard a Rocket* (BEAR) was launched aboard a sounding rocket in New Mexico in July 1989 [241]. The core of this experiment was an RFQ accelerator which produced an H^0 beam with an energy of about 1 MeV and a flux equivalent to a current of 10 mA. As in the L3 RFQ system, an H^- ion source and a gas cell neutralizer were used. The BEAR experiment was successful; however, the NPB weapon system does not appear to be practical in the near future [242]. Another interesting example of NPB applications can be found in fusion plasma experiments, where an injection of a neutral beam, typically with an energy of about 100 keV, is used as one the fundamental plasma heating methods [243].

During its six years of operation at L3, the RFQ calibration system proved to be robust and reliable, and the last calibration run performed in September 2000 showed no evidence of aging of the RFQ system hardware. Therefore, at the end of LEP program it was decided to move the RFQ system from the L3 cavern to a storage room at CERN. In January 2001 we successfully transferred the RFQ system together with all readout electronics to the designated storage area. Only minimal changes were made to the RFQ setup so that the system is ready to resume working. Figure B.1 shows the RFQ system after it was lifted from the L3 cavern.

Figure B.1: Photograph of the RFQ system taken prior to its transfer to the storage area. The beam pipe and the most downstream cryopump have already been removed. Standing in front of the system are members of the Caltech group involved in the RFQ dismantling, from left: M. Gataullin, S. Shevchenko, and X. Lei.

B.1 RFQ Accelerator System

The RFQ Accelerator System (RAS), shown in Figure 5.11, consists of the ion source, RFQ accelerator, high-energy beam transport, and neutralizer. The RAS was built by AccSys Technology Inc. [244] under the U.S. Department of Energy's Small Business Innovation Research program. It has been extensively modified and upgraded by the Caltech L3 group. Here I describe the RFQ system in its present configuration. The general system specifications are summarized in Table B.1.

To ensure proper internal alignment of the system, the RAS was mounted on a rigid frame (see Figures 5.11 and B.1). As shown in Figure 5.10, the RFQ target was located inside the BGO calorimeter and the RFQ frame was therefore tilted to an angle of about 22° with respect to the floor. The orientation of the most downstream cryopump was set by the requirement not to interfere with the sweep of the L3 magnet

1. Ion Source:	
Type	RF excited volume H^- source
Plasma Trigger	Hairpin filament
RF frequency and power	2 MHz, 30–50 kW
Extraction energy	30 keV
Pulse length and frequency	$50\mu s$, up to 150 Hz
Output H^- current	7.5 mA
2. RFQ Accelerator:	
Nominal output energy	1.85 MeV
Operating frequency	425 MHz
Beam pulse width	1–25 μsec
Beam repetition rate	1–150 Hz
Intervane voltage	65 kV
Maximum surface gradient	35 MV/m
Required RF power (peak)	200 kW minimum
Output beam current (peak)	up to 30 mA
Residual vacuum	$< 3 \times 10^{-6}$ Torr
Output energy spread (90%)	± 20 KeV
Transmission efficiency	$\simeq 75\%$
3. Neutralizer:	
Type	Gas (N_2) filled
Optimum pressure	5–9×10^{-4} Torr
Length and inside diameter	1 m, 40 mm
Efficiency	Up to 55%
Output H^0 flux (pulsed)	Up to 4 mA (equivalent)

Table B.1: Specifications of the RFQ accelerator system components: 1) ion source, 2) RFQ accelerator, and 3) neutralizer.

doors.

The RAS can produce beam pulses up to 50 μs of length with a repetition rate as high as 150 Hz. However, as explained in Section 5.6, it was typically run with a pulse length of about 5 μs and a repetition rate of 80 Hz.

B.1.1   Ion Source

The H^- ion source follows the RF-driven *volume* source design invented at LBL [245]. It was further developed and built by the AccSys Technology Inc. [244]. The ion
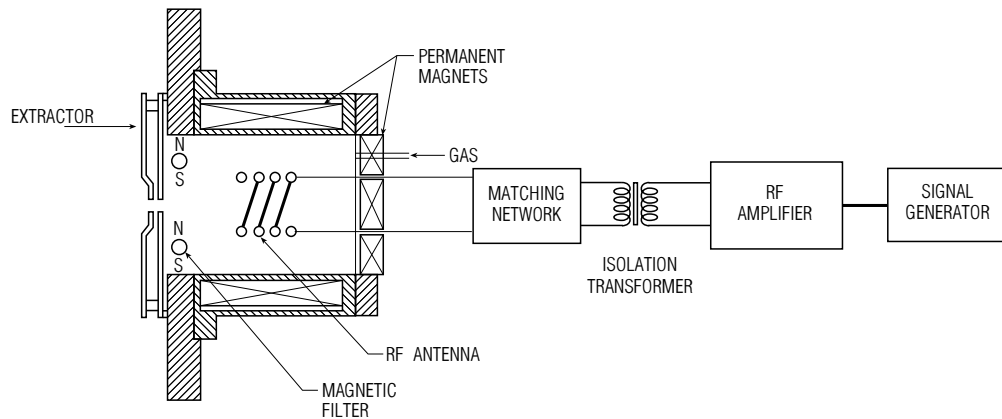
Figure B.2: A schematic showing the RF-driven H^- ion source.

source is compact and can be operated remotely for periods of several weeks with little or no maintenance. Meeting these requirements was essential for all elements of the L3 RFQ system, as the space allocated for the system was limited and the L3 cavern was not accessible during LEP operation. In addition, the RF-driven ion sources have a longer lifetime compared to the conventional ion sources driven by filament cathodes.

A schematic diagram of the ion source is shown in Figure B.2. The plasma chamber of the ion source is a copper bucket surrounded by columns of permanent magnets arranged in a longitudinal line cusp configuration. Its back flange also consists of permanent magnets that provide longitudinal confinement. Hydrogen is pumped into the chamber using a pulsed electromechanical valve and ionized using a helicoidal antenna. Typically, 30 to 50 kW pulsed 2 MHz RF power is fed to the antenna. The antenna is made out of 2.5 turns of glass-coated, 4 mm diameter, copper tubing and is cooled by water circulating in the tubing. A hot wire (hairpin filament) is used as a starter for the plasma. A 4 mm wide extraction aperture, opposite to the back flange, is separated from the the rest of the plasma chamber by a pair of water cooled permanent magnet rods. The magnet filter rods provide a transverse magnetic field of about 120 G, necessary to enhance the H^- yield [245].

The extraction of the negatively charged beam (populated mostly by electrons) is achieved by applying a -30 kV potential to the plasma bucket and grounding

the extraction electrodes. The extracted beam is decelerated to -14 kV and the e^- component (up to a few amperes) is removed using a magnetic spectrometer. The H^- beam is then re-accelerated to 30 keV and focused into the RFQ by an electrostatic lens. Since most of the ion source operates at -30 kV, it is isolated from the RF generator using a ferrite RF transformer and is connected to the RAS control system via an optical cable.

The obtained H^- current is typically about 7 mA, which requires a hydrogen gas flow of about 8 sccm to maintain the pressure in the plasma chamber at the optimum level of 35-40 mTorr. The hydrogen is evacuated by a 3 klps cryopump and the residual vacuum near the extraction electrodes is better than 5×10^{-6} Torr. The pressure in the plasma chamber is measured and controlled using a Pirani gauge.

As discussed in Section 5.6, the intensity of the RFQ calibration photon flux was well below the optimum level. Essentially this was because the H^- ion source of the RFQ system, the first commercial prototype in the world, was not capable of providing a large enough output current. The H^- current can be enhanced by introducing a trace amount of cesium in the extraction region of the source. An improved version of our ion source, built by the LBL group for the SSC laboratory, provided an output current of $70 - 100$ mA ($30 - 35$ mA without cesiation) [246].

B.1.2   RFQ Accelerator

The RFQ is a quasi-electrostatic accelerator, which offers advantages of a very compact size (typically 1-3 m long) and a high beam current (up to 100 mA). It derives its name from its use of radio-frequency voltages and quadrupole focusing [247]. Manufactured by AccSys Technology, the 1.85 MeV L3 RFQ accelerator is a 1.626 m long copper plated mild iron structure of a four vane type. It is tuned to a resonant frequency of 425 MHz and has a transmission efficiency of 75% for the injected 30 keV H^- beam. The L3 RFQ can be operated with a repetition frequency of $1 - 150$ Hz and its pulse length can be varied between 1 and 25 μs. The input RF power of 240 kW is provided by a three stage parallel planar triode array based on Varian Eimac tri-
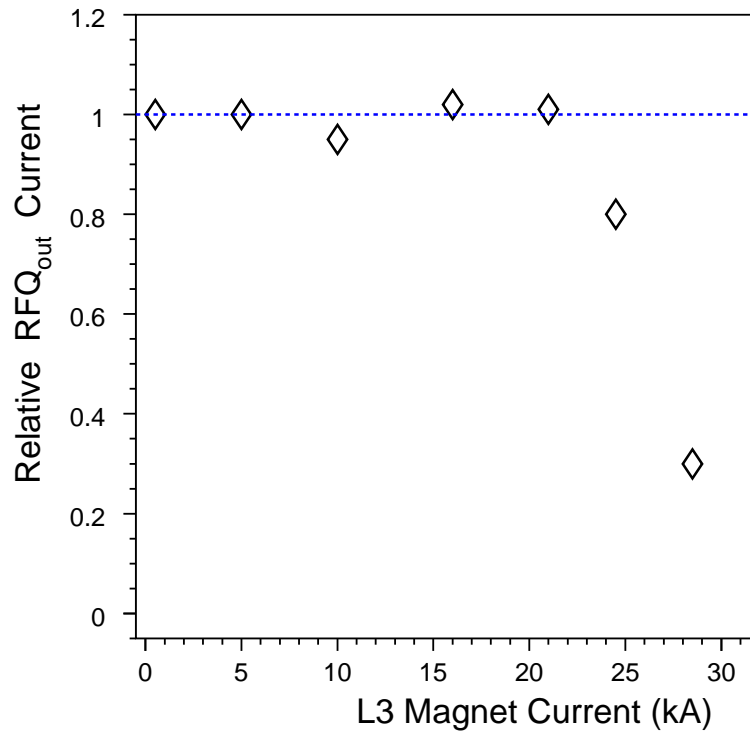
Figure B.3: Relative H$^-$ current from the RFQ accelerator as a function of the L3 magnet current. The nominal L3 magnet current was 30 kA.

ode tubes [248]. The RFQ is evacuated by a 1.5 klps cryopump which maintains the residual vacuum in the RFQ (with beam) below 1×10^{-6} Torr.

The output beam current from the RFQ is measured using a toroidal coil. Before entering the gas-cell neutralizer, the beam is focused and steered by a set of quadrupole and dipole magnets.

Magnetic Shielding

Early *in situ* tests of the RFQ system demonstrated that the output current from the RFQ accelerator decreased with the L3 magnet current. Figure B.3 shows that about 80% of the beam was lost at the nominal magnet current of 30 kA. The L3 spectrometer magnet (see Section 4.2.1) provided a field of 5 kG which was, however, well contained inside the detector. The fringe magnetic field near the RFQ site was measured to be $50 - 100$ G. After extensive calculations had shown that such a low

magnetic field could not affect the propagation of the H^- beam, it was realized that the soft iron RFQ vanes could concentrate the field in the intervane gaps, producing local fields substantially higher than expected. This effect was particularly severe at the input stage, where the resulting fields deflected most of the beam out of the acceptance range of the RFQ. The problem was solved by enclosing the ion source and the RFQ inside a shielding box made out of 15 mm thick soft-iron plates. With the magnetic shielding, the RFQ system proved to be completely insensitive to the fringe field and several RFQ calibration runs were successfully performed with the L3 magnet on.

Control System

The ion source and the RFQ amplifier were controlled with a PC installed with a MIL-STD-1553B standard controller board. The control program, written in Turbo Pascal, provided access to several I/O channels which could be configured without modifying the source code. All machine settings were transferred to the PC every few seconds. A system of software interlocks (in addition to the already existing hardware ones) was implemented to allow the user to ramp the high voltage while watching other critical machine parameters. The control system was also used to monitor and adjust the nitrogen pressure in the neutralizer cell. This was done by using a Perkin Elmer pressure controller, which allowed to adjust the gas flow through a piezoelectric valve.

B.1.3 Beam Neutralizer

The focused and steered H^- beam was neutralized in a N_2 gas cell ($H^- \rightarrow H^0 + e^-$) so that the neutral beam could pass undisturbed through the 0.5 T L3 magnetic field. The neutralizer consisted of two coaxial steel cylinders, each with a length of about 1 m. The inner cylinder had several hundred holes (diameter $\phi < 1$ mm) through which the nitrogen diffused into the central region. Two 3 klps cryopumps were used to evacuate the gas cell, one on each side. Thus, a dense gas column was maintained
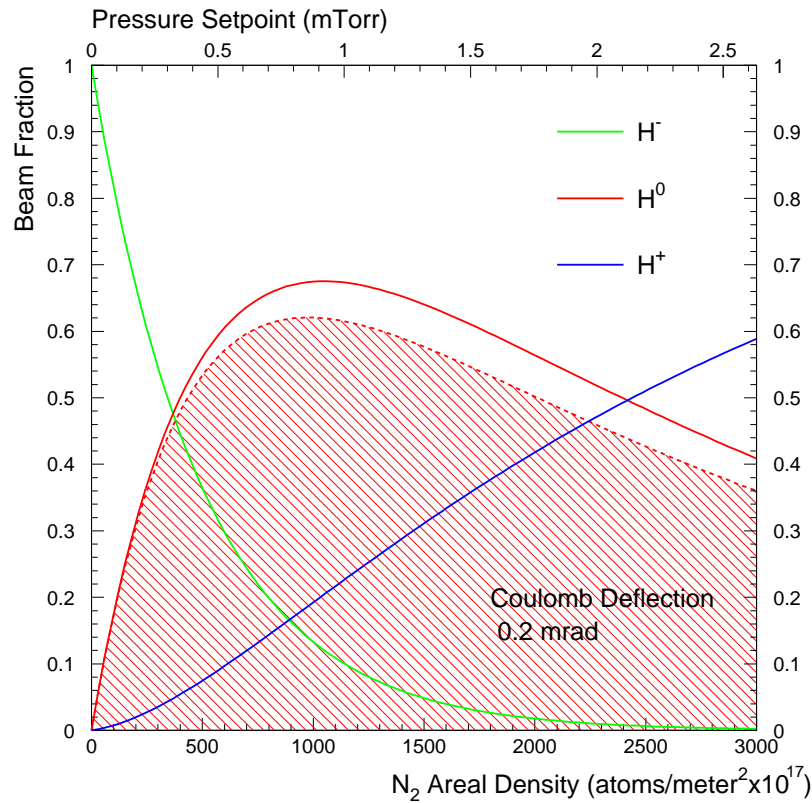
Figure B.4: Relative intensities of the H^-, H^0, and H^+ beams (after the neutralizer), calculated as functions of pressure in the gas cell. The hatched area represents the neutralization efficiency with the Coulomb scattering taken into account.

in the cell, while the pressure at the ends of the cell was below 1×10^{-6} Torr. The gas pressure in the inner cylinder was measured and the nitrogen flow into the outer cylinder was controlled using a piezoelectric valve.

At an optimum pressure of $0.6 - 0.9$ mTorr, the maximum neutralization efficiency of about 55% can be reached with this gas cell. This result is in good agreement with measurements performed with similar gas neutralizers [249]. Figure B.4 shows relative intensities of the H^-, H^0, and H^+ beams (after the neutralizer), calculated as functions of pressure in the gas cell.

B.2 Neutral Beam Transport

At this stage the beam was focused, steered, and neutralized, ready to be transported through a 10 m long beam pipe penetrating the L3 magnet, support tube, and calorimeters (see Figure 5.10) to reach a lithium target near one of the BGO endcaps. Figure 4.11 shows the location of the RFQ target and the end portion of the RFQ beam pipe with respect to the BGO calorimeter.

The RFQ neutral beam transport was made of two narrow tubes (inside diameter 40 mm). A manifold consisting of three KF-25 and one CF-40 flanges was mounted on the inner surface of the L3 support tube. One end of this manifold was attached to one of the tubes connected to the neutralizer, while the other end was connected to the other tube holding the target. Due to size limitations, the end portion of this tube was twice as narrow (inside diameter 20 mm). The beam pipe was electrically isolated from the rest of the RFQ system and its alignment was ensured using a dedicated laser system.

A 20 lps Varian StarCell ion pump mounted on the CF-40 flange of the manifold was used to evacuate the beam pipe. The ion pump was designed to be driven by the L3 magnetic field; however, a coil dipole magnet was also installed to allow the operation of the pump with the L3 magnet off. The dipole magnet produced a magnetic field of 850 G, which was sufficient to drive the ion pump at 60% of the maximum pumping speed. The vacuum in the beam pipe (with beam) was better than 5×10^{-6} Torr. Maintaining such high vacuum was necessary because the cross section of single electron loss by a hydrogen atom in nitrogen ($H^0 \to H^+ + e^-$) was quite large, about 6×10^{-17} cm^{-2} [250]. The energetic protons produced in this reaction would bend in the L3 magnetic field and hit the walls of the beam pipe. Such collisions produced unwanted radiative capture backgrounds and liberated thousands of gas molecules from the pipe's walls (outgassing), which in turn increased the pump load. This problem was mitigated by lining the last 80 cm of the beam pipe with a thin tantalum foil.

In general, the hydrogen atoms were lost in the neutral beam transport mainly
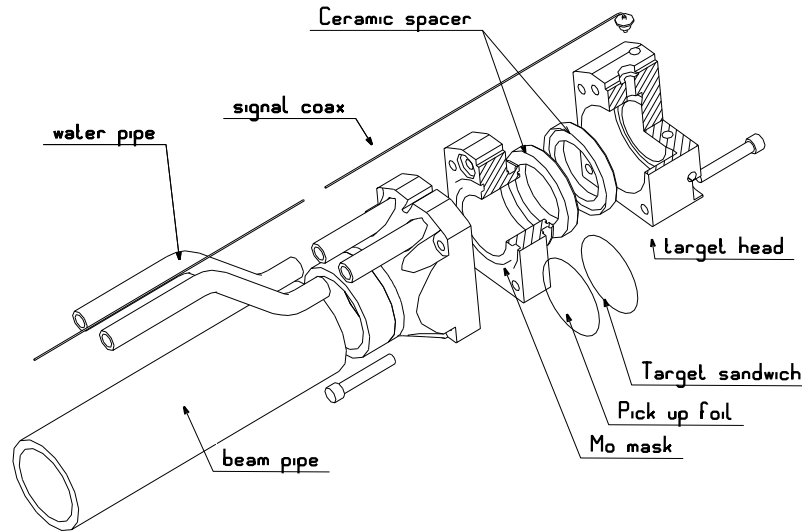
Figure B.5: The mechanical structure of the target.

because it was impossible to focus and steer the H^0 beam. The total beam loss was calculated to be about 50% and occurred mostly in the last portion of the beam pipe, which was forced to taper down due to the geometry of the BGO calorimeter.This result agreed well with a direct measurement of the H^0 beam intensity, which was carried out during one of the LEP shutdowns. The RFQ target was replaced with a specially designed Faraday cup, consisting of a 25 μm thick aluminum foil, a dipole magnet, and a charge collection plate. The foil was used to strip electrons from the incoming hydrogen atoms, while the secondary electrons were suppressed using the dipole magnet. The H^+ and H^- fractions of the beam were eliminated using another bending magnet installed after the neutralizer. The resulting H^+ current was measured to be about 1.5 mA or $\simeq$ 30% of the H^- current from the RFQ accelerator, consistent with the calculated losses due to neutralization (45%) and neutral beam transport (50%).

B.3   Target

The original design of the RFQ target is shown in Figure B.5. The target was made out of a 50 μm thick lithium foil sandwiched between two circular molybdenum or
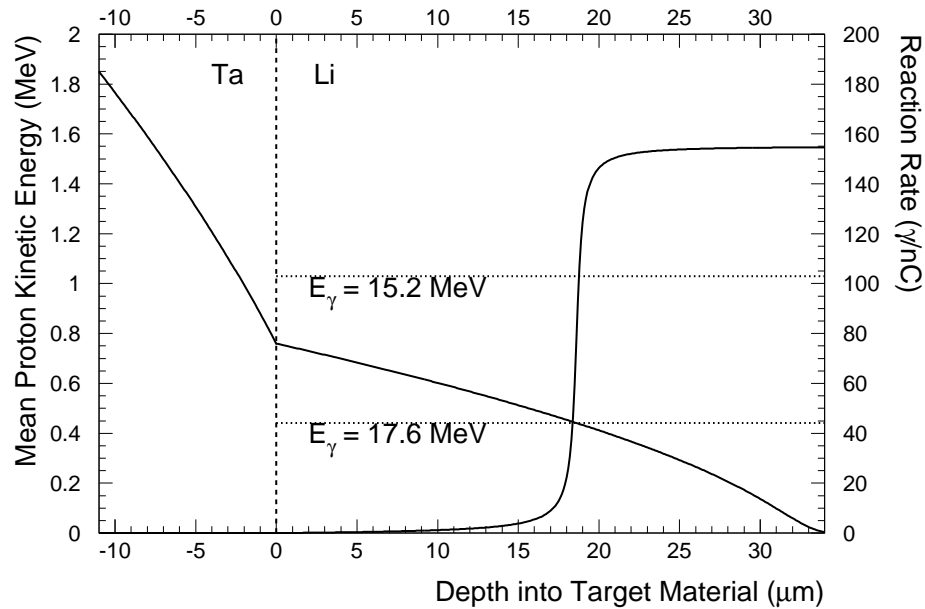
Figure B.6: Mean proton kinetic energy and proton radiative capture yield as functions of the depth into the target material. This plot shows calculations performed for a 11 μm thick tantalum foil. However, it is also approximately valid for a 12 μm molybdenum foil, as these metals have almost the same stopping power for 1 MeV protons: $dE/dx(\text{Ta}) = -105$ keV/μm and $dE/dx(\text{Mo}) = -97$ keV/μm [252].

tantalum foils (6 μm and 50 μm thick). To avoid oxidation of the lithium, the foils were hot-pressed (melted) together in a pure argon atmosphere. The foil sandwich was encapsulated in a water-cooled molybdenum holder with the 6 μm molybdenum foil facing the beam. Another 6 μm thick molybdenum foil was mounted on ceramic rings, about 2 mm upstream of the target. The molybdenum foils served two purposes:

(1) **As an energy degrader:** The reaction $^{7}_{3}\text{Li}(\text{p}, \gamma)$ $^{8}_{4}\text{Be}$ has a narrow resonance[1] at a proton energy of 441 keV and a broader resonance at about 1.03 MeV. These two resonances produce photons with different energies, 17.6 MeV and 15.2 MeV, respectively. Therefore, to produce a monochromatic calibration photon flux, the incoming protons had to be slowed down. As shown in Figure B.6, the molybdenum (or tantalum) foils reduced the beam energy from 1.85 MeV to

---

[1]This resonance has a width of $\Delta E_p = 12$ keV (FWHM) and the maximum cross section of about 6 mb [153, 251].

below 0.8 MeV. Protons then slowed down in the lithium, hitting the 441 keV resonance while avoiding the undesired resonance at 1.03 MeV.

(2) **As a Faraday cup:** The upstream foil was used to strip electrons from the incident hydrogen atoms. The resulting negative charge was measured, providing an estimate of the neutral beam intensity.

The molybdenum (or tantalum) foils were used because these metals are stable at high temperatures and have low radiative capture cross sections, thereby minimizing the unwanted γ ray background [150]. A 17.6 MeV photon yield of about 160 γ/nC was obtained with this target design.

In 1995 it was discovered that the molybdenum foils did not provide complete protection from the atmosphere and that, after a few months, the lithium would degrade into lithium hydroxide (LiOH). This effect reduced the photon yield from the target by almost 85%. Therefore the pure lithium foil was subsequently replaced with a pressed powder of lithium hydride (LiH), which was easy to handle and stable in dry air. Although the LiH target provided a photon yield of about half that of the original target design, it was preferred due to its long-term stability. In order to make the target sandwich sturdier, the two 6 μm thick molybdenum foils were replaced with a single 12 μm thick foil. Thus, the upstream foil was removed and the neutral beam was detected using other instruments as described in the next section.

B.4   Neutral Beam Detectors

The position and intensity of the steered H^0 beam was measured using two different instruments. The first one, a *single wire scatterer* (SWS), was based on the detection of protons produced by the Rutherford scattering of hydrogen atoms from a thin gold-plated tungsten wire (0.25 mm in diameter). The wire was mounted at the neutral beam transport manifold, about 5 m from the target, and oriented perpendicular to the beam direction. The scattered protons were detected using a small silicon surface barrier detector, which was installed on the inner surface of the manifold.

The resulting signal was used as a trigger for the RFQ data acquisition system. The SWS could also be used to focus the RFQ beam as the amplitude of its signal was proportional to the number of scattered hydrogen atoms.

In order to improve the neutral beam diagnostics and facilitate the tuning of the beam optics, a dedicated beam profile chamber was built in 1995. The chamber consisted of two orthogonal wire planes, each with 10 negatively biased sense wires interleaved with 11 ground wires. The 10 μm gold-plated tungsten wires were fixed on ceramic frames which were built using thick-film hybrid circuit technology. When the H^0 beam hit the sense wires, it knocked out secondary electrons that were repelled by the electric field created by the bias voltage. Therefore, a positive charge was left on the sense wires. Experimentally it was determined that this signal was proportional to the beam intensity and the cross-talk between the wires was negligible.

The charge deposited on the sense wires within 10 μs of the beam passage (typically 0.1 pC) was integrated and amplified by a preamplifier, the same as the ones used in the readout of the BGO calorimeter. After further amplification, the signal was transmitted to the counting room, where a sample-and-hold circuit produced a DC signal proportional to the collected charge and drove an LED display. The beam profile chamber was installed about 2 m upstream of the RFQ target, i.e., substantially closer than the SWS detector, and proved to be extremely useful for beam alignment.

B.5   Data Acquisition System

The RFQ runs were taken with the BGO calorimeter readout in the *local* standalone mode so that the BGO timing configuration was essentially the same as the one used during LEP data taking. The 5 μs RFQ beam pulse was tuned to arrive during the 11 μs integration window of the BGO. This was achieved by driving the RFQ accelerator system using the LEP beam-crossing time mark, which arrived with a period of 22 μs, and setting the BGO integration gate to start about 3 μs before the LEP time mark. The RFQ *trigger accept* signal was generated by the SWS neutral

beam detector. The trigger accept started the digitization of the BGO data and suspended the RFQ run. Once the BGO digitization process was complete, the RFQ system could be triggered by the next LEP time mark. With this timing scheme, an average readout speed of about 80 Hz was achieved, which was substantially faster than the L3 readout speed during the LEP runs (10 Hz).

The RFQ signals registered in the crystals were read out through the BGO token-passing network and further recorded by a specially designed online histogramming VHC module (Veto-Histogram-Counter). The VHC had a 256 channel histogram memory for 8192 crystals, so that only half of the BGO calorimeter was read out during each run. In order to reject BGO showers that were not contained in a single crystal, channels with hits in neighboring crystals were not histogrammed. The veto threshold for the neighboring hits was set to be equal to 1.5 σ above the pedestal. The threshold values were measured and updated before each RFQ run. The obtained histograms were then written to an RZ file which could be analyzed in PAW (*Physics Analysis Workstation*).

Appendix C

Studies of the BGO Performance

In this appendix I describe the technical aspects of my work on the calibration and monitoring of the BGO calorimeter. These include studies of the BGO non-linearity and aging, a special procedure that I developed to treat BGO showers with dead or missing crystals, and a description of the Crystal Ball lineshape fit. In addition, I also present the angular resolution functions for electromagnetic showers measured in both the barrel and endcap regions of the calorimeter.

C.1   Crystal Ball Lineshape Fit

As discussed in Section 5.6.2, the energy spectra of Bhabha electrons had a significant low-energy tail due to initial state radiation and, thus, could not be adequately described by a simple Gaussian distribution. In order to take this effect into account, I fitted the Bhabha spectra to the Crystal Ball lineshape (CBL) function.[1] This composite function consists of two parts, a Gaussian peak and a power-law tail, and is given by the following formula:

$$
\Psi(E \,|\, E_p, \sigma, A, a, r) =
\begin{cases}
A \cdot \exp\left[\dfrac{-(E - E_p)^2}{2\sigma^2}\right] & \text{if } E > E_p - a\,\sigma \\[4mm]
A \cdot \left(\dfrac{b}{a}\right)^b \dfrac{\exp(-a^2/2)}{\left[(E_p - E)/\sigma + \frac{b}{a} - a\right]^b} & \text{if } E \leq E_p - a\,\sigma,
\end{cases}
$$

(C.1)

where E is the observed energy, E_p is the position of the peak, σ is the width of the peak, A gives the overall normalization, and a and b are the parameters describing

---

[1] This function was originally used by the Crystal Ball experiment to fit the energy response of its NaI(Tl) crystal calorimeter [152]. In L3, the CBL function was also used to fit the distributions of the forward-backward charge asymmetry in Bhabha scattering [135].
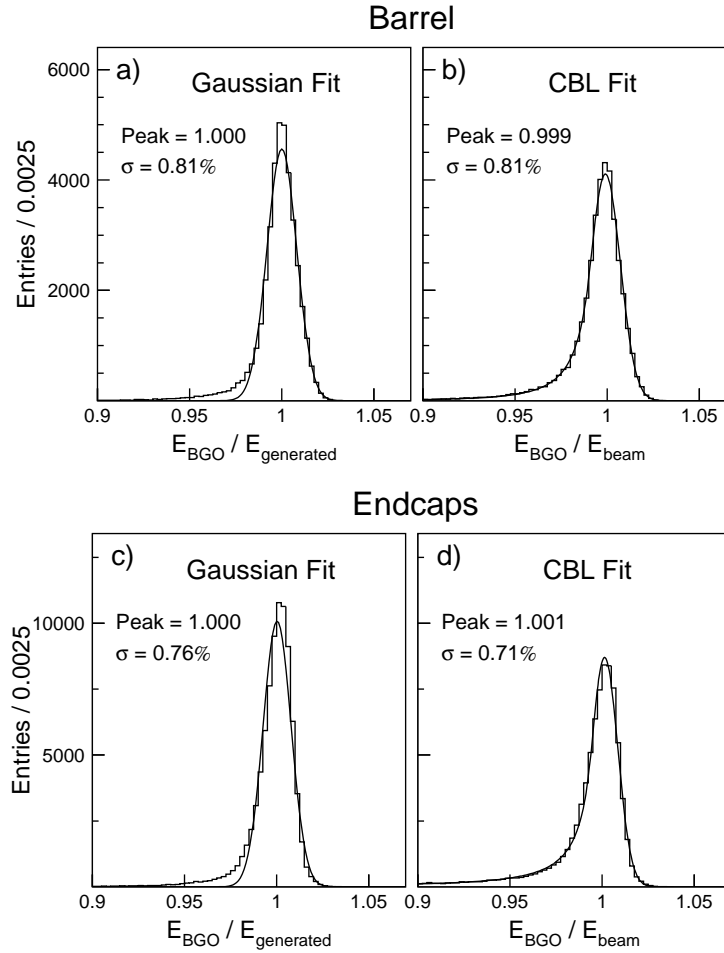
Barrel

Endcaps

Figure C.1: Comparison between (a,c) the Gaussian and (b,d) the Crystal Ball lineshape fits to the distributions of the E_{BGO}/E_{gen} and E_{BGO}/E_{beam} variables, respectively. The obtained peak positions and resolutions are indicated on the plots. There are two entries per each MC event.

the power-law tail, where a defines the joining point and b gives the power. The above formula automatically ensures that both parts of the CBL function join continuously and are smooth in the first derivative. For the Bhabha energy spectra at LEP, the fitted values of the parameters a and b were in the ranges $1 < a < 2$ and $1.5 < b < 3$.

I studied the performance of the CBL fit using a sample of 70,000 back-to-back Bhabha events which I selected from a Monte Carlo sample generated at the Z peak, $\sqrt{s} = 91.3$ GeV, where the shower development in the BGO had been simulated assuming a perfect calibration and no temperature fit errors. Figures C.1a,c show the distributions of E_{BGO}/E_{gen}, where E_{BGO} is the reconstructed energy of the BGO

bump and E_{gen} gives the energy of the corresponding electron at the generator level. As can be seen, these distributions could be reasonably well fitted with a single Gaussian function, despite a noticeable low-energy tail caused by fluctuations in the shower development process (e.g., shower leakage effects or energy losses in the dead material between the crystals). The fitted width of the peak was then taken as the intrinsic energy resolution of the BGO calorimeter.

For the data, the true value of the electron energy (E_{gen}) was of course unknown and, to determine the energy resolution of the BGO, I had to use another variable, E_{BGO}/E_{beam}, where E_{beam} is the beam energy. The corresponding distributions fitted to the CBL function are shown in Figures C.1b,d.

Comparing the fitted values of the peak position and width obtained with these two methods, good agreement was observed in all cases. In addition, for both the data and Monte Carlo spectra, the fitted CBL curves provided a good description not only for the peak region but also for the the low-energy tail as can be seen from Figures C.1b,d and 5.20. Thus, it could be concluded that the Crystal Ball lineshape function worked well in fits to Bhabha energy spectra and provided a consistent estimate of the BGO energy resolution.

C.2   Showers with Dead or Missing Crystals

As discussed in Section 5.3.2, about 1.5% of the BGO channels were malfunctioning (*dead*) and therefore were not used in the shower reconstruction. In addition, the BGO calorimeter had six rings of crystals at the edges of the calorimeter, one in each half-barrel and two in each endcap. As a result, about 12% of the selected single-photon showers contained a dead channel in the 3×3 matrix around the crystal with the maximum energy deposition (bump crystal), and for additional 5% of the showers, the bump crystal was in one of the edge rings so that the 3×3 matrix contained three *missing* crystals. Such showers were also used in the absolute calibration of the BGO in order to calibrate crystals adjacent to the dead crystals and crystals near the detector edges.

	$\phi-1$	ϕ	$\phi+1$
$\theta+1$	1.8 %	6.3 %	1.8 %
θ	6.3 %	67.5 %	6.3 %
$\theta-1$	1.8 %	6.3 %	1.8 %

	$\phi-1$	ϕ	$\phi+1$
	I	II	I
	II	B	II
	I	II	I

Figure C.2: **Left:** Average energy fractions in the 3×3 crystal matrix for the bumps with no dead or missing crystals (for 45 GeV electrons). **Right:** Definition of the Type I and Type II BGO bumps, where "B" denotes the bump crystal and "I" and "II" denote the possible positions of the dead crystals.

The standard BGO reconstruction algorithm treated the dead and missing crystals as crystals with zero energy depositions, resulting in a systematic underestimation of the measured bump energy. This effect was then accounted for by disabling the corresponding crystals during the Monte Carlo simulations of the BGO calorimeter. However, for some applications this approach proved to be insufficient. For example, the absolute calibration of the BGO was based on the assumption that the reconstructed electron energies in the back-to-back Bhabha events should be close to beam energy.

In order to correct for the presence of the dead and missing crystals, I used the following procedure.[2] First, the BGO bumps with missing or dead crystals were divided into three categories. The *Type* I bumps contained a dead crystal in one of the four corners of the 3×3 matrix, while for the *Type* II bumps, the dead crystal was

---

[2]This problem has also been investigated in 1997-98, and an alternative shower fitting procedure was developed [253] It was shown that this algorithm provided a substantial improvement in the reconstruction quality for the BGO bumps with dead or missing crystals. However, it also produced significant resolution tails and, thus, was not used in my analysis (or in any other L3 analyses).

Parameter	Type I		Type II		Type III	
	Barrel	Endcaps	Barrel	Endcaps	Barrel	Endcaps
P_{Data} [%]	98.4 ± 0.3	98.4 ± 0.3	97.3 ± 0.3	97.8 ± 0.2	96.4 ± 0.2	96.8 ± 0.2
P_{MC} [%]	98.6 ± 0.1	98.7 ± 0.2	97.6 ± 0.1	98.0 ± 0.1	96.8 ± 0.2	97.1 ± 0.1
σ_{Data} [%]	1.4	1.5	1.6	1.5	2.3	2.0
σ_{MC} [%]	1.6	1.6	1.7	1.5	2.3	2.1

Table C.1: Results of the CBL fits to the E_{bump}/E_{beam} distributions for the bumps with missing or dead crystals. Peak positions and resolutions are listed both for the data, P_{Data} and σ_{Data}, and Monte Carlo, P_{MC} and σ_{MC}.

adjacent to the bump crystal (see Figure C.2). The *Type* III bumps were the showers near the edges of the BGO which contained three missing crystals in the 3×3 crystal matrix. This particular classification was motivated by fact that the average energy loss in dead or missing crystals was different for each type of such bumps. Figure C.2 shows that for Type I showers, the systematic underestimation of the measured bump energy was expected to be substantially smaller than for bumps of Type II and III.

To estimate the systematic negative shift in the measured bump energy, I used back-to-back Bhabha events selected from a Monte Carlo sample generated at the Z peak, $\sqrt{s} = 91.3$ GeV, where the calibration and temperature fit errors had been taken into account during the detector simulation. The selection criteria that I used are listed in Section 5.6.2. It should be noted that the selected bumps had to satisfy the quality cuts on the shower shape, which rejected a significant fraction of Type II and Type III bumps. As a consequence, about 40% of the selected bumps with dead or missing crystals were of Type I and the rest was divided equally between the Types II and III.

The Bhabha energy spectra were fitted to the CBL function, and the fit results are given in Table C.1. The obtained correction factors were then applied during the absolute calibration of the BGO. To test this correction procedure, I used a sample of bumps with dead or missing crystals that were selected in the Z-peak calibration data collected from 1998 to 2000. Figure C.3 shows the Bhabha energy spectra for the

Dead Channels of Type I   Dead Channels of Type II
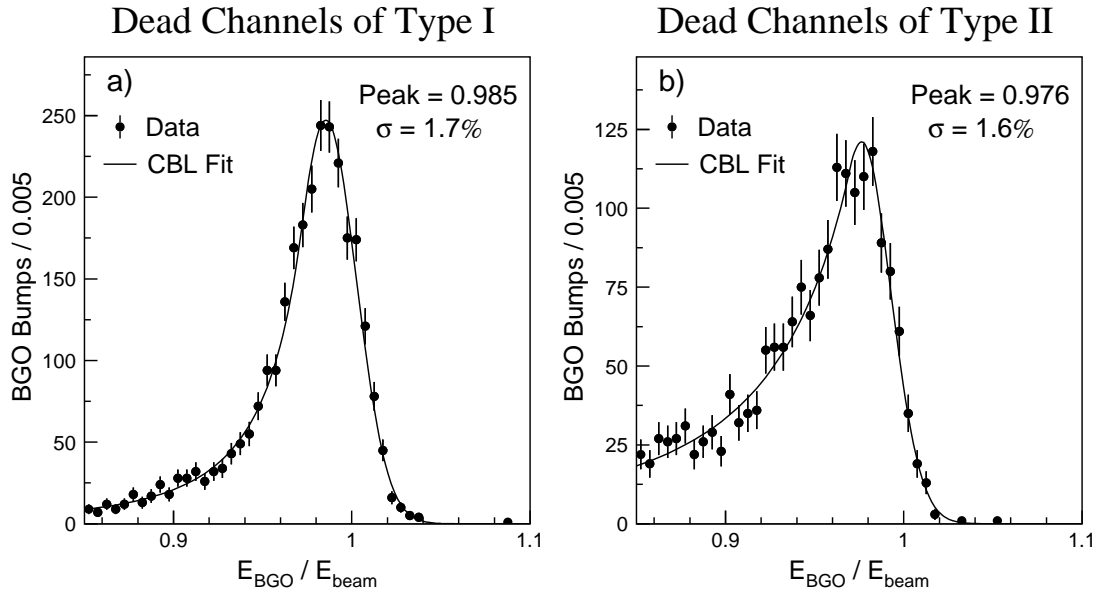

Figure C.3: Energy spectra of the Bhabha electrons selected in the 1998-2000 Z-peak calibration data a) for the BGO bumps of Type I and b) for the BGO bumps of Type II (barrel and endcaps combined). The peak positions and resolutions are indicated on the plots.

BGO bumps of Type I and II, and the fitted parameter values are listed in Table C.1. Comparing the fitted values of the peak position and width, good agreement between the data and Monte Carlo was observed in all cases. For 45 GeV electrons, the BGO energy resolution was measured to be about 1.5% for bumps of Type I and II and about 2% for bumps of Type III.

The shower-shape cuts that I used in the selection of the single- and multi-photon events were identical to the cuts used in the Bhabha selection. Therefore, the same correction procedure could also be applied to the selected single- and multi-photon samples. As shown in Figure 6.21f, this procedure corrected the position of the recoil-mass peak for the single-photon showers containing dead or missing crystals.

C.3   Aging of the BGO Calorimeter

At the beginning of the LEP program in 1989, it was noticed that the BGO response decreased with time at a rate of 2-3% per year. The BGO aging was then extensively
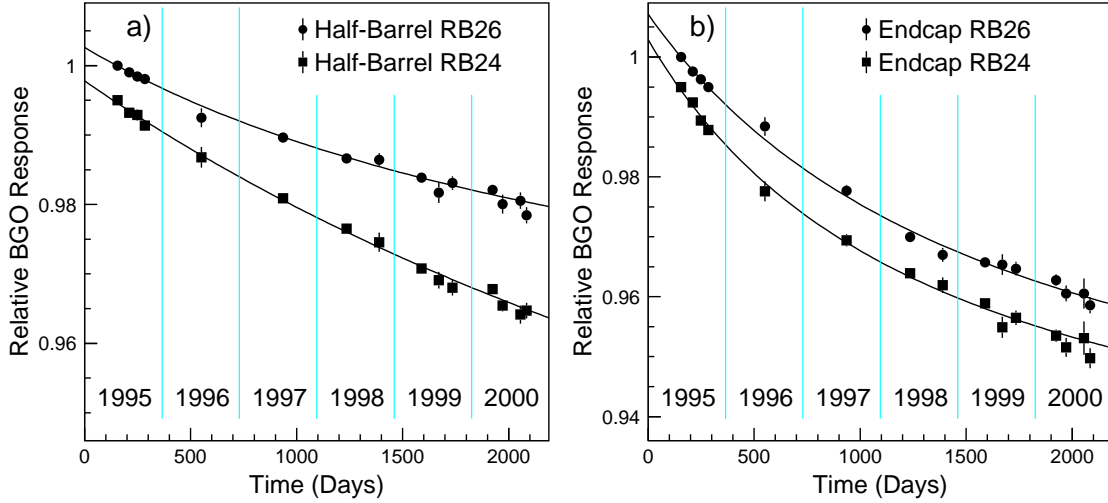
Figure C.4: Aging of the BGO during 1995-2000 a) for the two half-barrels and b) for the two endcaps. Each point represents a LEP run at or near the Z peak, $\sqrt{s} \simeq 91.3$ GeV. For better visibility, the aging curves for the RB24 side are shifted by -0.5%.

studied using the Xenon monitoring system and it was found that, fortunately, the decay rate also decreased with time [139, 134]. The measured decay trend could be parameterized by

$$R(t) = \frac{a}{t - t_0} + C, \tag{C.2}$$

where R is the relative BGO response, t is the elapsed time, and a, t_0, and C are constant parameters. Since the four subdetectors of the BGO were manufactured and installed separately, the decay functions $R(t)$ were different for each subdetector.

In order to estimate the BGO aging during the LEP2 phase, I used the back-to-back Bhabha events selected in the Z-peak calibration data.[3] Typically, during each year of the LEP2 program, two or three weeks were dedicated to LEP runs at the Z peak, $\sqrt{s} = 91.3$ GeV. For example, in 1999 such runs were performed in May, July, and September, and the L3 detector collected a total of about 4.0 pb^{-1} of the Z-peak calibration data. The Bhabha energy spectra from each calibration run[4] were then

---

[3]Using only electrons of fixed energy, 45.6 GeV, avoided the problem of the BGO non-linearity (see the next section).

[4]To avoid potential biases, energies of all Bhabha showers were reconstructed using the same set of the RFQ intercalibration constants.

fitted to the CBL function, and the BGO aging curves were obtained by plotting the fitted peak position versus the elapsed time (see Figure C.4).

The decay rate was higher in the endcaps because they were installed two years after the barrel calorimeter. As shown in Figure C.4, the aging of all four BGO sub-detectors was well described by the parameterization of Equation C.2. The obtained aging curves were then used for both the BGO calibration and the BGO reconstruction. At the end of the LEP2 program, the relative energy response of the BGO changed by about -0.4% per year for the barrel and by about -0.6% per year for the endcaps. These results were in good agreement with a similar study carried out using the Xenon monitoring system [140].

Although the exact cause of aging of the BGO is unknown, it is suspected to be due to the degradation of the reflective paint which was used to coat the BGO crystals. The L3 LUMI detector made of non-coated BGO crystals did not exhibit any significant aging effects. Radiation damage could be excluded as a cause because the radiation flux of LEP peaked at low polar angles, while the rate of aging was uniform within a given BGO subdetector. Moreover, the measured radiation flux was very low [254].

C.4   Non-linearity of the BGO Calorimeter

In general, any electromagnetic calorimeter is expected to have a linear energy response, i.e., the measured shower energy should be proportional to the energy of the incident photon (electron). However, in practice, deviations from the signal linearity (*non-linearity*) can be caused by a variety of instrumental effects such as the light attenuation or shower leakage effects [108].

During the LEP1 program, the BGO non-linearity was studied using multi-GeV electrons where the bump energy measured in the BGO was compared to the momentum of the corresponding charged track reconstructed in the TEC (E/p) [139]. It was found that the relative energy response of the BGO changed by about 0.5% when going from 5 GeV to 45 GeV [149]. Because this effect was not reproduced by
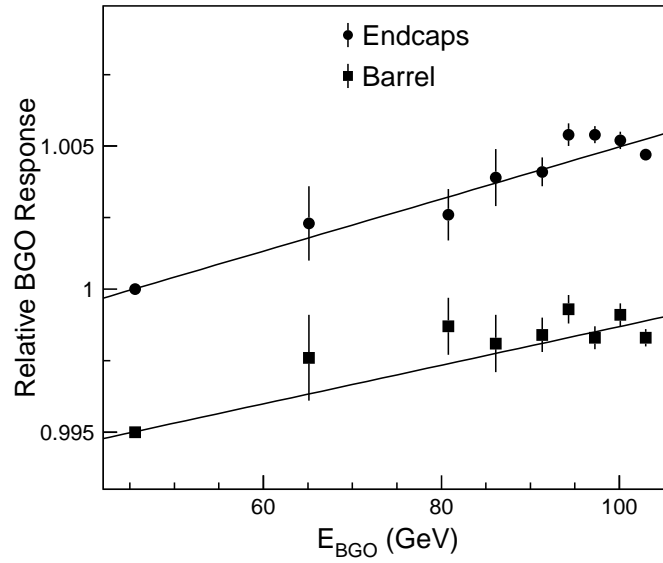
Figure C.5: Energy dependence of the BGO energy response. For better visibility, the non-linearity curve for the barrel is shifted by -0.5%.

the Monte Carlo simulations, the corresponding correction factors were included in the energy reconstruction algorithm of the BGO. For lower shower energies, the BGO non-linearity could be precisely studied using the mass peaks of the π^0 and η mesons reconstructed in their two-photon decay mode (see Section 5.6.3).

During the years 1995-2000, the LEP beam energy was gradually increased from 46 GeV up to 104 GeV. Thus, Bhabha samples selected at different center-of-mass energies could be used to investigate the linearity of the BGO response. For a given beam energy, I measured the BGO non-linearity by comparing the position of the corresponding Bhabha peak to the position of the Bhabha peak from the closest (in time) Z-peak calibration run.[5] The obtained non-linearity curves are shown in Figure C.5. The corresponding shift in the relative BGO response was measured to be about 0.5% for both the barrel and the endcaps, confirming the general trend observed at LEP1. Again, this behavior was not reproduced by the Monte Carlo simulations, and the corresponding correction factors were included in the energy reconstruction algorithm of the BGO.

---

[5]To avoid potential biases, the shower energies were reconstructed using the previous year's calibration, i.e., the data under investigation were not used to derive the corresponding calibration constants.

C.5   BGO Angular Resolution

As described in Section 5.1, the impact point of the incident particles was reconstructed using the energy depositions in the 3×3 crystal matrix and the actual positions of the crystal front faces (θ_i and ϕ_i). The corresponding angular resolution functions were derived in Reference [110] and are given by:

ϕ-Resolution:

Barrel

$$\sigma_\phi^B(E) = \frac{3.28 \text{ mrad}}{\sqrt{E}} + 0.82 \text{ mrad} \quad (E \text{ in GeV}) . \tag{C.3}$$

Endcaps

$$\sigma_\phi^E(E, \theta) = (1.21 \, \sigma_\phi^B(E) + 2.56 \text{ mrad}) \left(\frac{4.76/|\tan \theta| + 3.81}{4.76/|\tan \theta_{ref}| + 3.81} \right) , \tag{C.4}$$

where $\tan \theta_{ref} = 523 \text{ } mm/758 \text{ } mm$ corresponds to the intersection of the barrel and endcap volumes.

θ-Resolution:

Barrel

$$\sigma_\theta^B(E, \theta) = \sigma_\phi^B(E) \left(\frac{5.55 \sin \theta + 1.21}{5.55 \sin \theta_0 + 1.21} \right) , \quad \theta_0 = \frac{\pi}{2} . \tag{C.5}$$

Endcaps

$$\sigma_\theta^E(E, \theta) = (0.77 \, \sigma_\phi^B(E) + 0.99 \text{ mrad}) \left(\frac{6.06|\cos \theta| + 0.66}{6.06|\cos \theta_{ref}| + 0.66} \right) , \tag{C.6}$$

where the reference polar angle θ_{ref} is the same as in the expression for $\sigma_\phi^B(E)$ (Equation C.3). The longitudinal section of the BGO calorimeter (see Figure 4.11) was a rectangle, and therefore only the barrel ϕ-resolution function did not depend on the polar angle of the shower. In addition, since the BGO granularity was almost the same in the barrel and in the endcaps, the remaining resolution functions could be parameterized in terms of $\sigma_\phi^B(E)$ and θ.

   As a cross check, I derived the ϕ-resolution function for the barrel using a Monte Carlo sample of single-photon events. Figure C.6a shows that it was in good agree-
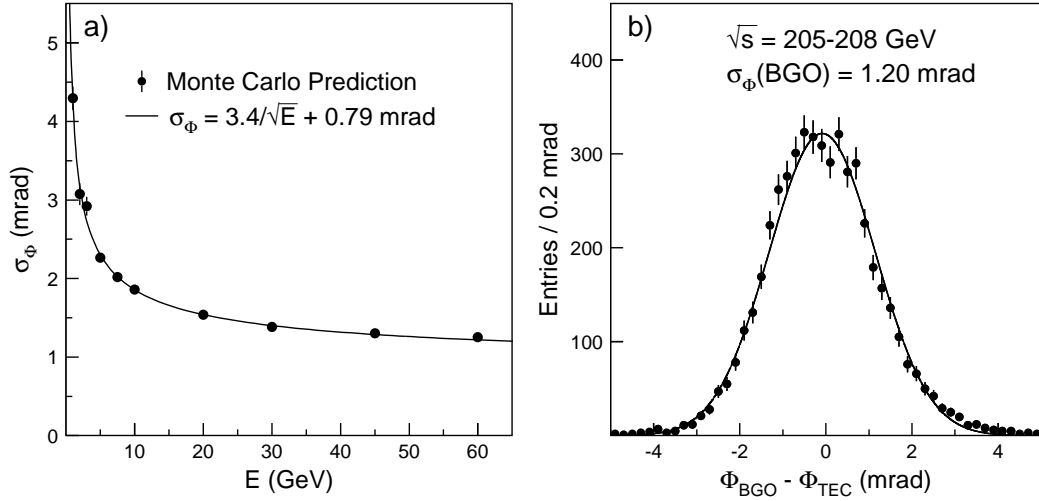
Figure C.6: a) BGO angular resolution as a function of the shower energy, as predicted by the Monte Carlo simulations. b) ϕ-resolution for the barrel measured using 103 GeV Bhabha electrons (two entries per event).

ment with the function $\sigma_\phi^B(E)$ given by Equation C.3.

For electrons in the barrel region, a much more precise measurement of the azimuthal angle was obtained by reconstructing the associated charged track using the TEC and SMD subdetectors of L3 ($\sigma_\phi(\text{TEC}) \simeq 0.4$ mrad). The ϕ-resolution of the BGO could then be estimated by comparing the azimuthal angle measured by the BGO and by the TEC (see Figure C.6b). The measured value of $\sigma_\phi^B(\text{Data}) = 1.17 \pm 0.02$ mrad was in good agreement with the Monte Carlo prediction of $\sigma_\phi^B(\text{MC}) = 1.15$ mrad. This result was also confirmed by a similar study described in Reference [140].

Appendix D

Additional Results of the Event Selection

In this appendix I provide additional figures and tables that further illustrate the results of the event selections described in Chapter 6.

Figure D.1a shows the energy spectrum of the single-photon candidates. Figures D.1b and D.1c show the transverse momentum distributions of the single-photon candidates in the barrel and endcaps, respectively. These plots complement the main results of the single-photon selection, described in detail Section 6.3.8 of Chapter 6.

Figures D.2 and D.3 show the recoil mass distributions of the single-photon and multi-photon events with missing energy, respectively, collected at different center-of-mass energies. Figure D.4 provides the energy spectra of the soft-photon candidates collected at different center-of-mass energies. These plots are of interest because production cross sections of most new physics signals increase with the center-of-mass energy of e^+e^- collisions.

The results of the single- and multi-photon selections are detailed in Tables D.1 and D.2, respectively. In addition, Table D.3 gives detailed results of the combined single- and soft-photon selections in the region of $x_\gamma < 0.5$, where x_γ is defined as the ratio of the photon energy to the beam energy.

The accessible format of these tables ensures that they can be used by any interested physicist[1] to test future models involving single- and multi-photon signatures at LEP. Table D.3 has already been used to search for branon production [200] and is currently used to search for several exotic SUSY signatures at LEP [256].

---

[1] These three tables were included in the final L3 paper on single- and multi-photon production at LEP [230] as part of the general data-archiving effort of L3. To a large extent, this effort was motivated by a recent example from the JADE experiment at PETRA e^+e^- collider. In 1998, twelve years after PETRA's shutdown, the JADE collaboration had to overcome significant difficulties in order to reanalyze its data with new theoretical models and improved analysis techniques [255].
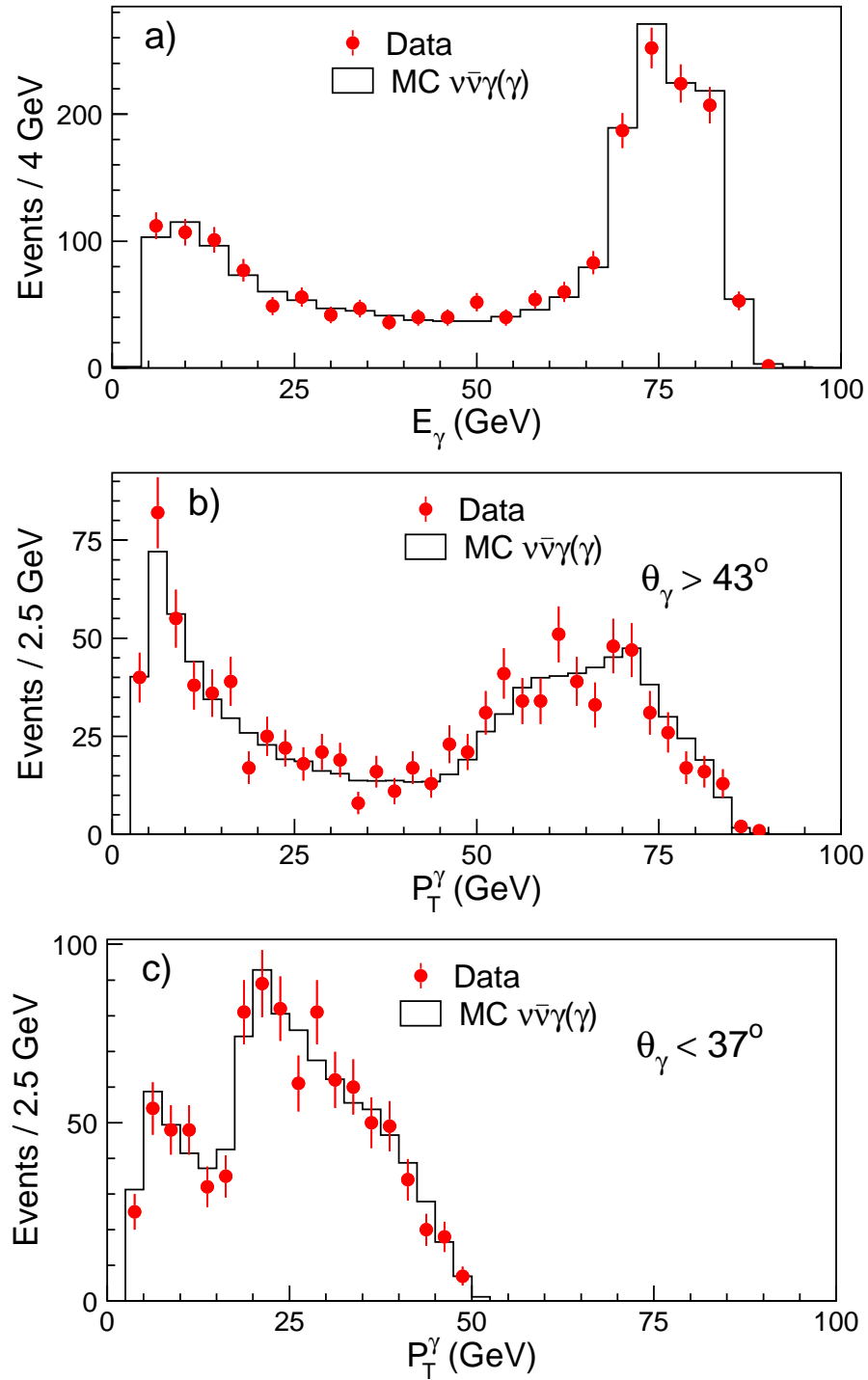
Figure D.1: a) Energy spectrum for the entire single-photon sample and transverse momentum distributions of the single-photon candidates b) in the barrel and c) in the endcaps.
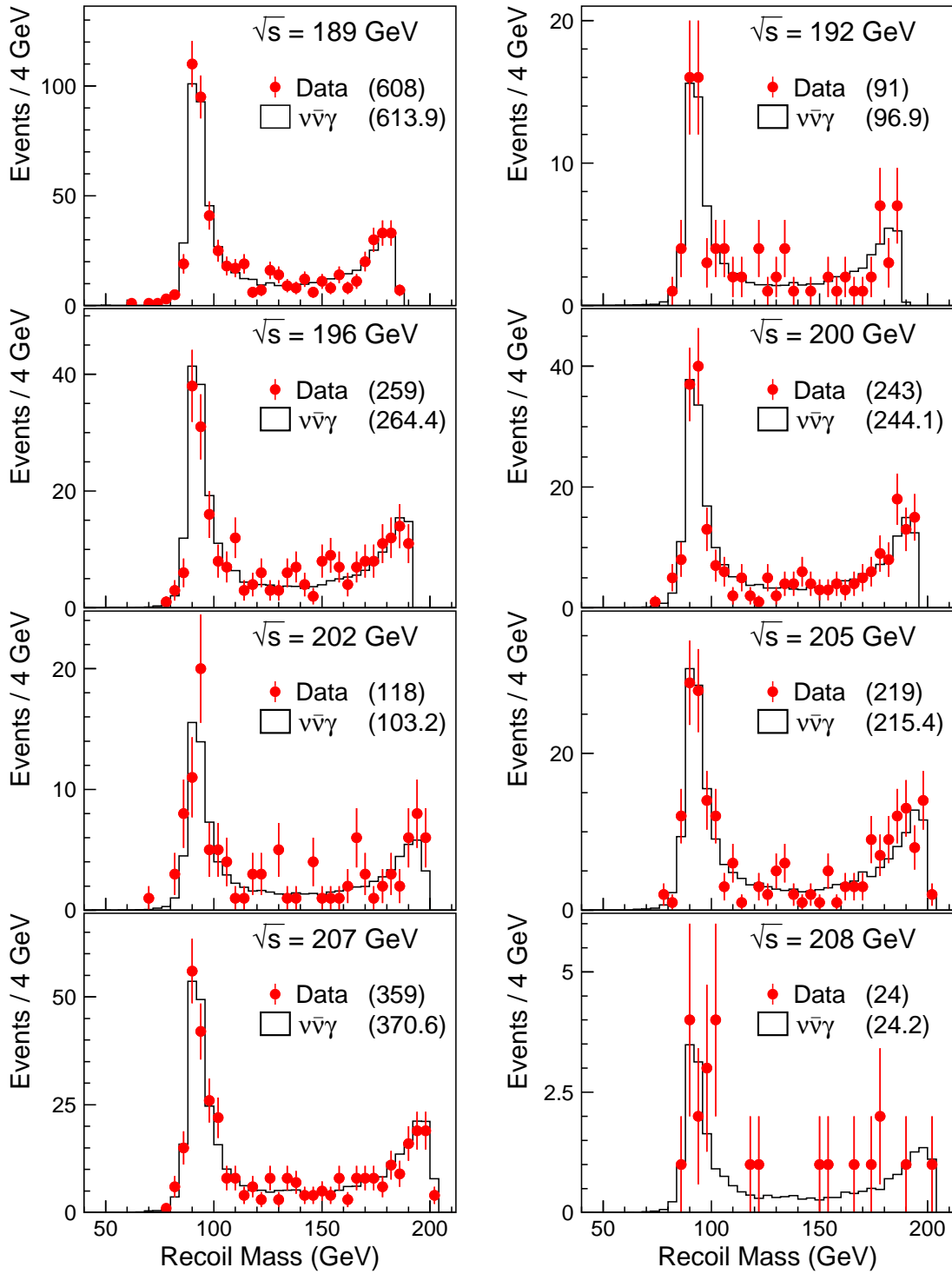
Figure D.2: Recoil mass distributions for the single-photon samples collected at different center-of-mass energies. The event statistics and values of $\sqrt{s}$ are indicated on the plots.
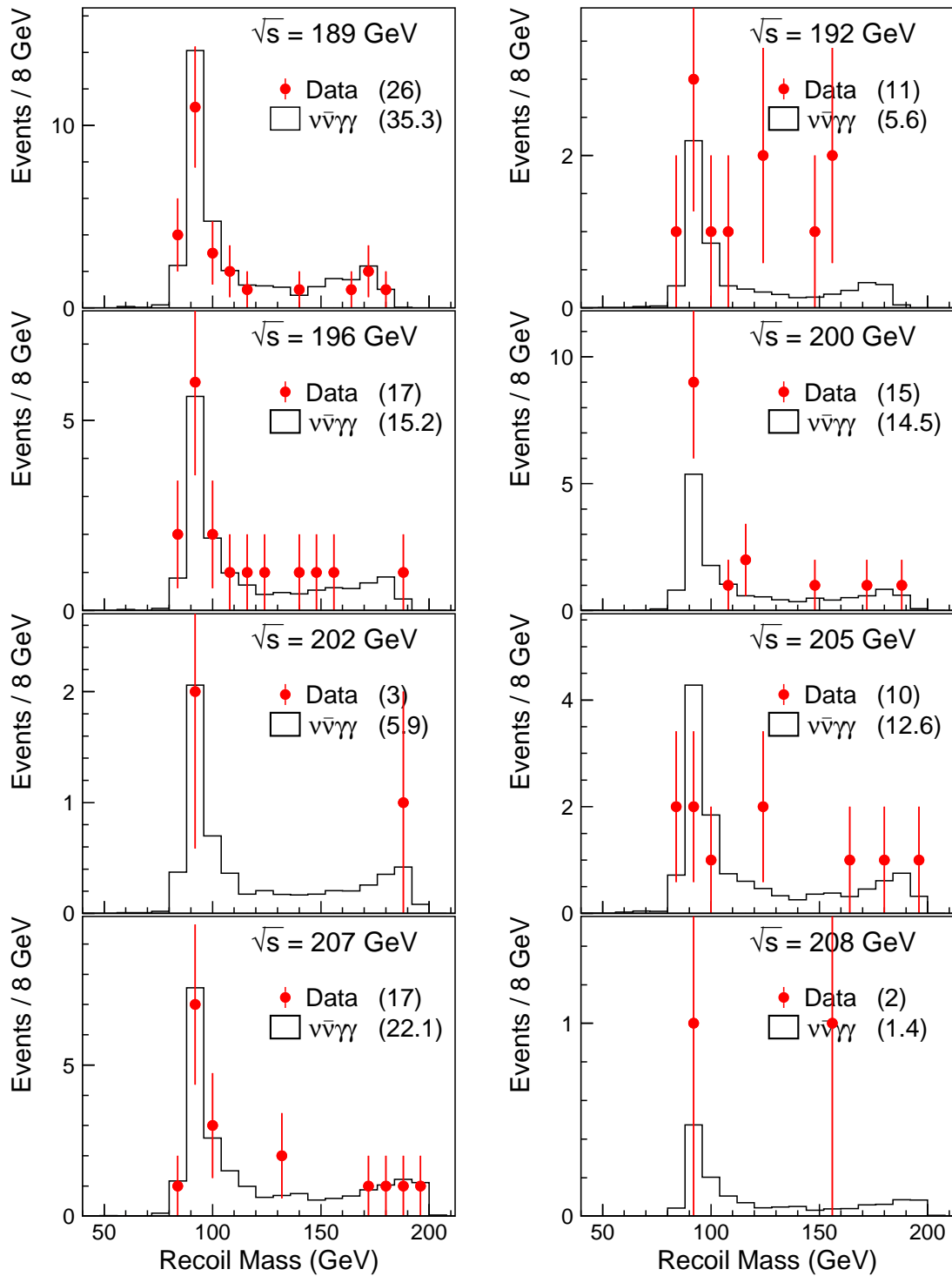
Figure D.3: Recoil mass distributions for the multi-photon samples collected at different center-of-mass energies. The event statistics and values of $\sqrt{s}$ are indicated on the plots.
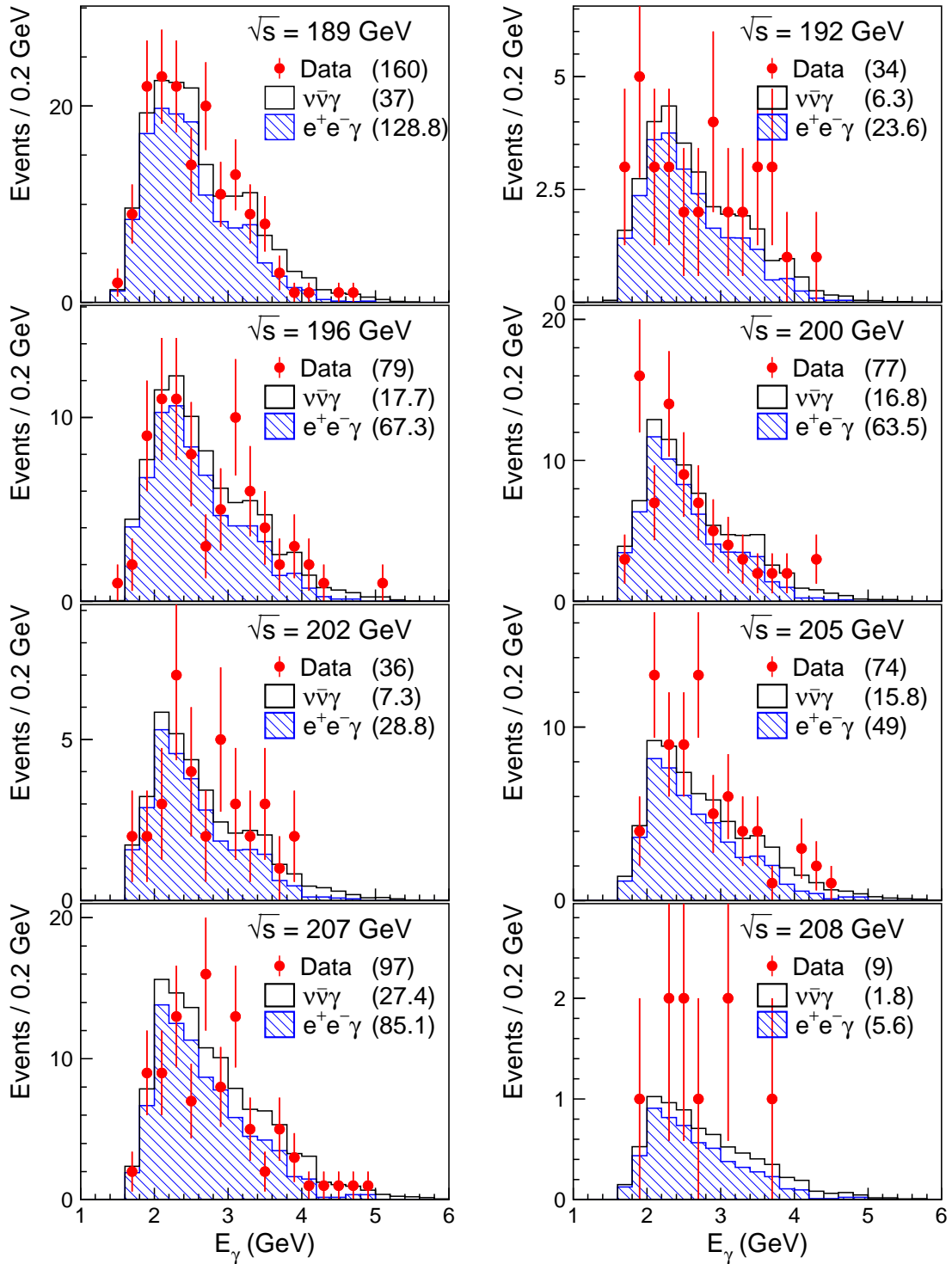
Figure D.4: Photon energy spectra for the soft-photon samples collected at different center-of-mass energies. The event statistics and values of $\sqrt{s}$ are indicated on the plots.

Table D.1: Number of events accepted by the single-photon selection in the 1998-2000 data, Standard Model expectations, and selection efficiencies (KKMC) in % as functions of the recoil mass and photon polar angle.

$|\cos\theta_\gamma|$	$M_{\rm rec}$ [GeV]					
	$0-70$	$70-95$	$95-120$	$120-145$	$145-170$	$170-210$
$0.000-0.200$	1/0.5/83	58/55.9/89	34/37.7/89	15/16.4/89	26/23.7/83	66/75.4/74
$0.200-0.400$	1/0.4/81	52/67.4/91	46/40.3/90	30/16.8/87	23/25.7/84	93/80.9/75
$0.400-0.600$	0/0.5/82	74/84.3/89	53/54.7/89	23/22.0/89	33/32.8/85	91/91.3/74
$0.600-0.730$	0/0.4/80	87/69.4/85	45/54.5/85	28/20.0/84	26/29.4/81	80/71.3/71
$0.800-0.870$	0/0.6/81	83/85.3/95	59/60.5/94	28/26.3/92	23/31.7/86	67/60.2/75
$0.870-0.920$	0/0.5/77	108/95.1/92	55/65.8/91	25/25.5/88	30/33.2/79	52/51.1/70
$0.920-0.953$	0/0.5/61	95/98.2/88	64/71.2/85	28/24.9/80	20/25.7/59	30/33.1/55
$0.953-0.972$	0/0.4/60	85/80.4/71	47/52.2/68	24/20.2/63	12/16.1/36	1/ 2.4/ 6

$M_{\rm rec}$ [GeV]	$E_{\gamma 2}$ [GeV]		
	$0 - 15$	$15 - 40$	$40 - 80$
Full sample			
$0 - 70$	0/ 0.2/62	0/ 0.1/66	0/0.2/64
$70 - 95$	38/30.7/64	12/12.4/53	0/1.5/57
$95 - 120$	15/21.7/65	5/ 7.9/56	0/0.4/53
$120 - 150$	9/10.2/60	2/ 2.5/51	—
$150 - 180$	13/16.8/54	0/ 0.7/46	—
$180 - 210$	7/ 7.4/41	—	—
Both Photons in Barrel ($43° < \theta_\gamma < 137°$)			
$0 - 70$	0/0.0/81	0/0.0/80	0/0.2/75
$70 - 95$	5/6.1/82	6/3.3/78	0/0.7/80
$95 - 120$	4/4.7/87	1/2.0/84	0/0.1/83
$120 - 150$	2/2.1/77	0/0.6/53	—
$150 - 180$	2/4.1/66	0/0.2/38	—
$180 - 210$	1/2.2/52	—	—

Table D.2: Numbers of observed and expected multi-photon events and selection efficiencies (KKMC) in % as functions of $E_{\gamma 2}$ and $M_{\rm rec}$ for the full sample and for the case in which both photons were in the barrel. These results are given for the combined 1998-2000 data sample.

x_γ	$\lvert\cos\theta_\gamma\rvert$					
	$0-0.2$	$0.2-0.4$	$0.4-0.6$	$0.6-0.73$	$0.73-0.92$	$0.92-0.972$
$0.00-0.02$	29 / 20.0	31 / 30.6	19 / 17.4	—	—	—
	30 / 18	36 / 12	39 / 12	—	—	—
$0.02-0.03$	39 / 39.6	58 / 53.2	111 / 112.7	111 / 129.9	—	—
	54 / 31	54 / 25	51 / 13	53 / 9	—	—
$0.03-0.05$	25 / 20.8	27 / 23.9	55 / 57.2	82 / 91.6	—	—
	65 / 88	62 / 83	62 / 42	60 / 23	—	—
$0.05-0.10$	28 / 28.7	36 / 30.3	36 / 37.1	31 / 31.0	12 / 18.1	—
	69 / 100	70 / 100	68 / 98	63 / 95	17 / 96	—
$0.10-0.20$	22 / 29.6	36 / 32.6	44 / 38.4	34 / 32.9	82 / 68.6	17 / 23.3
	79 / 100	81 / 100	80 / 100	75 / 99	74 / 99	21 / 93
$0.20-0.35$	24 / 22.7	21 / 25.6	28 / 30.5	34 / 27.2	43 / 57.7	24 / 30.4
	82 / 100	83 / 99	84 / 100	81 / 100	79 / 99	38 / 100
$0.35-0.50$	13 / 14.3	17 / 15.3	21 / 19.9	17 / 17.8	49 / 42.5	30 / 32.6
	84 / 100	86 / 100	86 / 99	80 / 100	86 / 99	59 / 100

Table D.3: Numbers of observed and expected single-photon events together with selection efficiencies and purities in % as functions of $\lvert\cos\theta_\gamma\rvert$ and of the ratio of the photon energy to the beam energy, x_γ. Results of the single- and soft-photon selections are combined for $x_\gamma < 0.5$. In the first row of each cell the left number represents the number of observed events and the right number the expectations from Standard Model processes. In the second row of each cell the left number is the selection efficiency (KKMC) and the right number is the purity. These results are given for the combined 1998-2000 data sample.

Appendix E

Combinations with Other LEP Experiments

The other three LEP experiments — ALEPH, DELPHI, and OPAL — have also studied the production of photonic events with missing energy and published descriptions of their work [111, 215, 216]. In this appendix I present the combinations of LEP results on the searches for photonic signatures expected in Supersymmetry and in models with extra dimensions. The LEP−combined samples of single- and multi-photon events with missing energy are also described. These combinations have been performed in the framework of the LEP SUSY [231] and Exotica [232] working groups, of which I am a member.

While the general designs of the LEP experiments were quite similar, the details varied significantly. In particular, the L3 BGO calorimeter stood prominently as the most accurate photon detector at LEP. Starting from 1997, the BGO calorimeter was precisely calibrated with the RFQ accelerator, which significantly improved its resolution and eliminated the resolution tails (see Chapter 5). The BGO energy resolution was about 1% for photons with energies above 10 GeV, at least three times as good as the resolution of any other electromagnetic calorimeter at LEP (see Section 4.2.3 p. 80).

In addition, the high-performance forward calorimeters of L3 allowed me to extend my single-photon selection to include photons with transverse momenta as low as 1.5 GeV (see Section 6.5). For comparison, the other LEP experiments had to apply a threshold cut of $P_t^\gamma \geq 5-7$ GeV. This resulted in L3 having a significantly higher sensitivity for detecting extra dimensions and pair-produced gravitinos.

For these reasons, the L3 experiment was the ideal place at LEP to search for new physics in photonic final states. As I will show below, the sensitivity of the
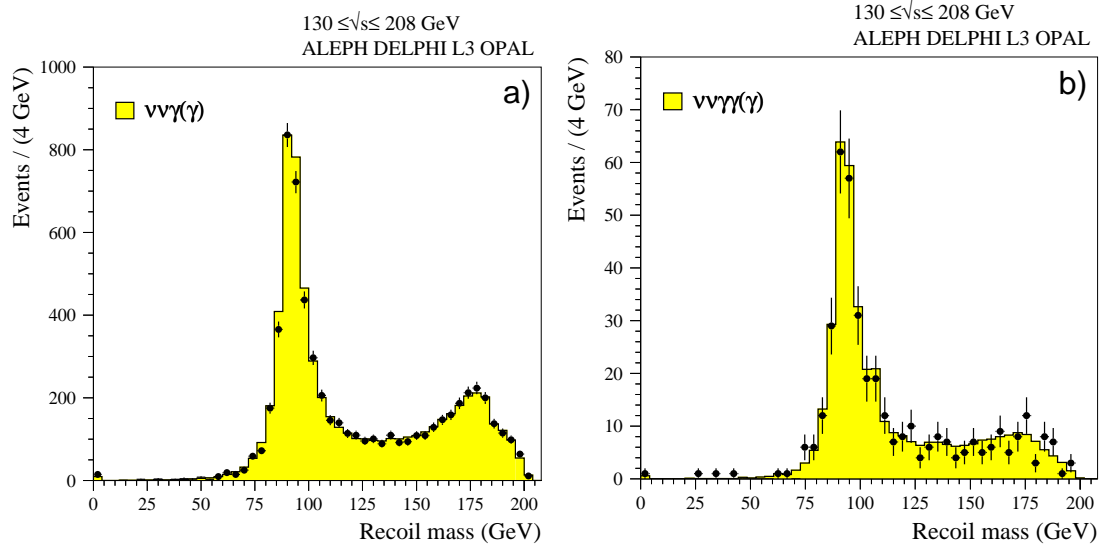
Figure E.1: Recoil mass spectra of the a) single-photon and b) multi-photon events selected by the four LEP experiments (points with error bars). The shaded histograms represent the Standard Model expectations.

LEP−combined searches for SUSY and extra dimensions was essentially the same as the sensitivity of my searches described in Sections 7.2 and 7.3. Moreover, the limits that I derived were almost always tighter than the limits obtained by combining the results from the other three LEP experiments.

E.1   The LEP Combined Event Samples

The combinations presented here are based on the results obtained with single- and multi-photon events selected by the four LEP experiments. These event samples have been selected in the data recorded during 1996-2000 from e^+e^- collisions at $\sqrt{s} = 161-208$ GeV, which corresponded to about 700 pb^{-1} per experiment. The only exception is the single-photon sample from OPAL which includes only events selected in about 250 pb^{-1} of data collected during 1996-1998 at $\sqrt{s} = 161 - 189$ GeV.[1] The combined single- and multi-photon samples consist of 6,282 and 392 events, respectively, with 6,424 and 406.3 events expected from Standard Model processes, mainly $e^+e^- \to \nu\bar{\nu}\gamma(\gamma)$. The corresponding recoil mass spectra are shown in Figure E.1.

---

[1] The OPAL experiment has not released any results from its single-photon analysis performed with 450 pb^{-1} of data collected in 1999-2000 at $\sqrt{s} = 192 - 208$ GeV.

M_{rec} [GeV]	Single-photon sample				Multi-photon sample			
	LEP		L3		LEP		L3	
	Data	MC	Data	MC	Data	MC	Data	MC
$0-70$	103	100.6	2	3.8	6	5.1	0	0.4
$70-110$	3272	3408.9	968	985.2	241	251.0	66	68.9
$110-160$	1350	1378.7	391	375.9	87	91.0	20	23.4
$160-210$	1557	1535.8	560	567.9	58	59.3	15	19.9
Total	6282	6424.1	1921	1932.7	392	406.3	101	112.7

Table E.1: Numbers of observed and expected events as a function of the recoil mass for the LEP−combined single- and multi-photon samples. For comparison, also given are the corresponding numbers for my samples selected using the L3 data collected at $\sqrt{s} = 189 - 208$ GeV.

Table E.1 gives the numbers of observed and expected events as functions of the recoil mass variable. For comparison, I also list the results of my single- and multi-photon selections performed using 619 pb^{-1} of data collected by L3 at $\sqrt{s} = 189 - 208$ GeV. In total, the L3 contributions represent about 35% and 30% of the LEP combined single- and multi-photon samples, respectively.

For the single-photon channel, there is good overall agreement between the LEP data and the Standard Model predictions. However, a noticeable deficit of events was observed in the region corresponding to the radiative return to the Z. In the bin $M_{\mathrm{rec}} = 70 - 110$ GeV, 3,272 events were found in the data while 3,408.9 were expected from the $\mathrm{e^+e^-} \to \nu\bar{\nu}\gamma$ process. This corresponds to a deficit of about $-2.3\,\sigma$.

Much of this lack of data was caused by the contributions from DELPHI and OPAL, which both used the `KORALZ` Monte Carlo generator for the simulation of the $\mathrm{e^+e^-} \to \nu\bar{\nu}\gamma$ process. However, the more advanced and precise `KKMC` program predicts 2-3% less events in the region of the Z-return peak (see Section 2.2.3). In addition, the DELPHI analysis suffered from significant systematic errors due to trigger inefficiencies and calorimeter calibration.[2] It should be noted that the ALEPH

---

[2]For the DELPHI analysis [216], the total systematic error on the measured cross section was about 5%, whereas for my analysis it was only about 1%.

and L3[3] single-photon analyses found a good agreement (within $0.5\,\sigma$) between the data and Monte Carlo in this region of the recoil mass spectrum. These two analyses were performed using the KKMC event generator and represented about 65% of the LEP−combined event sample.

The event statistics given in Table E.1 show that the other single-photon selections suffered from significantly higher backgrounds in the region of low recoil masses (high photon energies). Such background was mainly caused by the mismeasurement of events in the Z-return peak of the $e^+e^- \rightarrow \nu\bar{\nu}\gamma$ process. In my analysis, this source of background was found to be negligible because the RFQ calibration technique eliminated the BGO resolution tails (see Figure 5.9 p. 105). Only 3.8 $\nu\bar{\nu}\gamma$ events were expected in the bin $M_{\mathrm{rec}} < 70$ GeV, at least five times lower than for any other single-photon analysis performed at LEP. For this reason, the sensitivity of my searches for neutralino production processes in SUSY was substantially higher since such processes were expected to lead to events with energetic photons (see Sections 7.2.2 and 7.2.3).

For the multi-photon channel, good agreement between the data and Monte Carlo was observed for the entire recoil mass spectrum as shown in Figure E.1b. This combination is considered to be final since all four experiments provided their published results based on the full LEP2 data set.

E.2 Searches for SUSY Signatures

To perform combinations of LEP results on searches for Supersymmetry, the LEP SUSY working group adopted the following procedure. For a given signal hypothesis, each experiment provided the number of observed events, the number of expected background events, and the selection efficiency for this signal process. This information was then used to perform a multi-channel likelihood fit, and the cross section limits were derived using the *Fast Fourier Transform* method [257].

This procedure was suitable for the combination of results from other LEP ex-

---

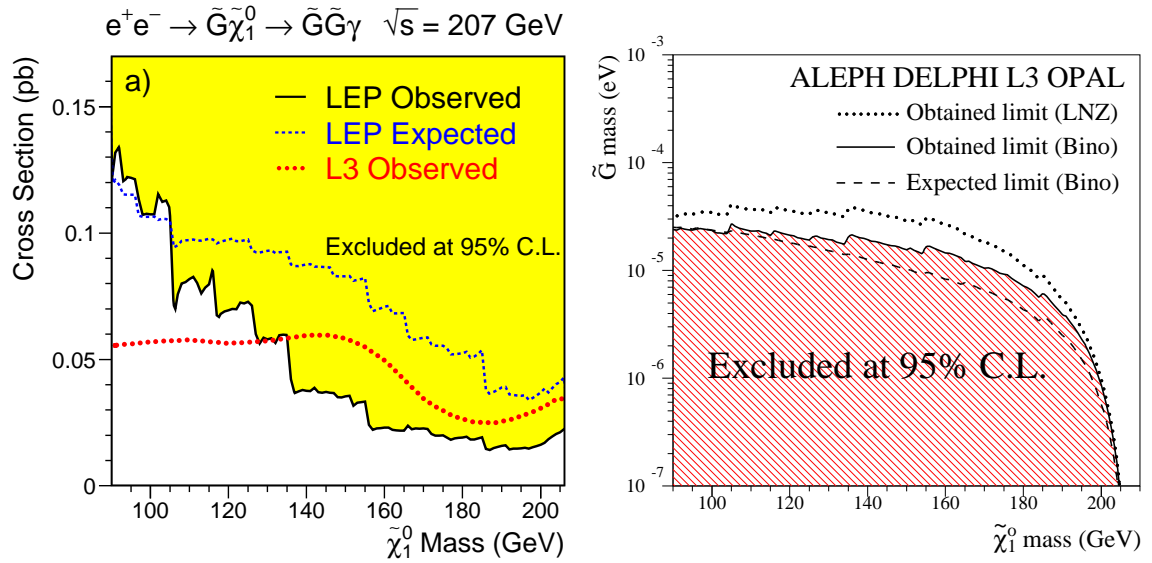[3]Here and in the following the L3 results refer to those described in this thesis.

Figure E.2: **a)** Observed and expected upper limits on the production cross section of the reaction $e^+e^- \to \tilde{G}\tilde{\chi}_1^0 \to \tilde{G}\tilde{G}\gamma$, obtained from the LEP−combined search. The corresponding limits from my search are also shown. The limits were obtained at the 95% C.L. for $\sqrt{s} = 207$ GeV. Data collected at lower $\sqrt{s}$ were included assuming the signal cross section to scale according to the LNZ model [193]. **b)** Regions excluded in the $(m_{\tilde{\chi}_1^0}, m_{\tilde{G}})$ mass plane, under the assumptions of the LNZ model and a pure bino neutralino GMSB model with $m_{\tilde{e}_R} = 150$ GeV.

periments which employed event-counting methods [111, 215, 216]. However, my searches for new physics were based on likelihood fits to discriminating distributions as described in Section 7.2.1. In order to provide the required information, e.g., just one number of observed events, I had to apply additional cuts on the discriminating variables. Although I optimized the values of these cuts, for some mass hypotheses this led to a significant deterioration of the analysis performance. As a consequence, the sensitivity of the LEP−combined search could become lower than the sensitivity of my individual search.

Figure E.2a shows the observed and expected upper limits on the signal cross section obtained from the LEP−combined search for the $e^+e^- \to \tilde{G}\tilde{\chi}_1^0 \to \tilde{G}\tilde{G}\gamma$ process. For high neutralino masses $m_{\tilde{\chi}_1^0} \geq 110$ GeV, the obtained limits were found to be significantly better than expected. This effect was caused by a substantial deficit of data events observed by the ALEPH analysis [111] in the region of highest sensitivity,
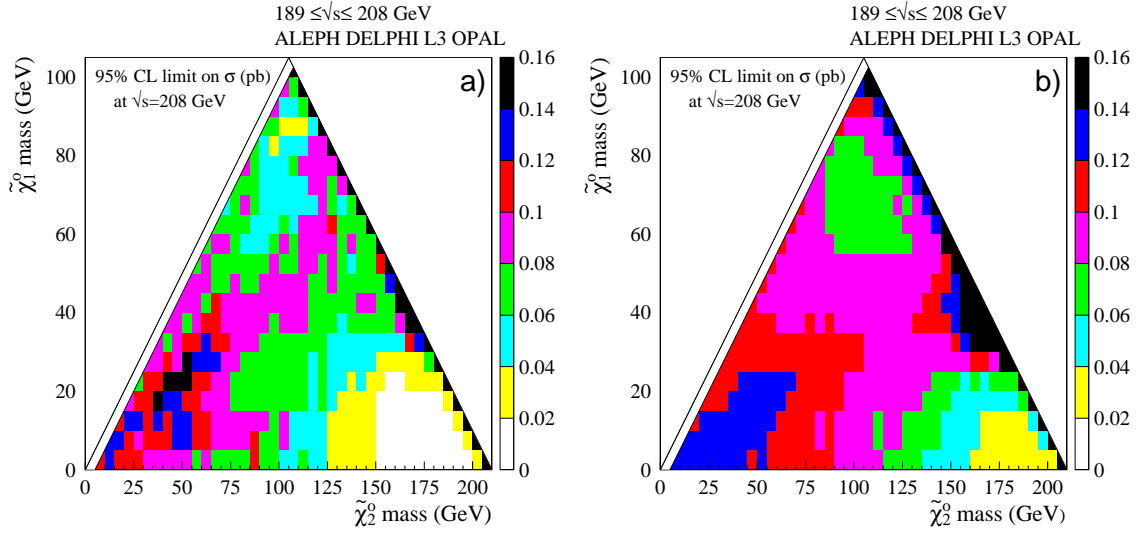
Figure E.3: a) Observed and b) expected cross section upper limits from the LEP−combined search for the process $e^+e^- \to \tilde{\chi}_2^0 \tilde{\chi}_1^0 \to \tilde{\chi}_1^0 \tilde{\chi}_1^0 \gamma$. The limits were obtained at the 95% C.L. for $\sqrt{s} = 208$ GeV. The branching fraction for the $\tilde{\chi}_2^0 \to \tilde{\chi}_1^0 \gamma$ decay was assumed to be 100%.

$M_{\rm rec} \lesssim 80$ GeV. Figure E.2a also shows the cross section limits that I derived in Section 7.2.2. The L3 and LEP−combined searches were found to have essentially the same sensitivity.

The no-scale SUGRA LNZ model has only two free parameters — the gravitino and the neutralino masses (see Section 3.2.4). Figure E.2b shows the exclusion region in the $(m_{\tilde{\chi}_1^0}, m_{\tilde{G}})$ mass plane obtained from this combination of LEP results. Gravitino masses below 10^{-5} eV were excluded for neutralino masses below 185 GeV.

The LEP−combined search for the reaction $e^+e^- \to \tilde{\chi}_2^0 \tilde{\chi}_1^0 \to \tilde{\chi}_1^0 \tilde{\chi}_1^0 \gamma$ was also performed. The observed and expected limits are shown in Figure E.3.

Multi-Photon Signatures

Figure E.4a shows the upper limits on the signal cross section obtained from the LEP−combined search for the $e^+e^- \to \tilde{\chi}_1^0 \tilde{\chi}_1^0 \to \tilde{G}\tilde{G}\gamma\gamma$ process. In this case, the observed limits were in good agreement with the expectation. Figure E.4a also shows the limits on the $e^+e^- \to \tilde{\chi}_1^0 \tilde{\chi}_1^0$ cross section that I derived from my search (Section 7.2.3). For neutralino masses above 85 GeV, the LEP−combined search was found to be more
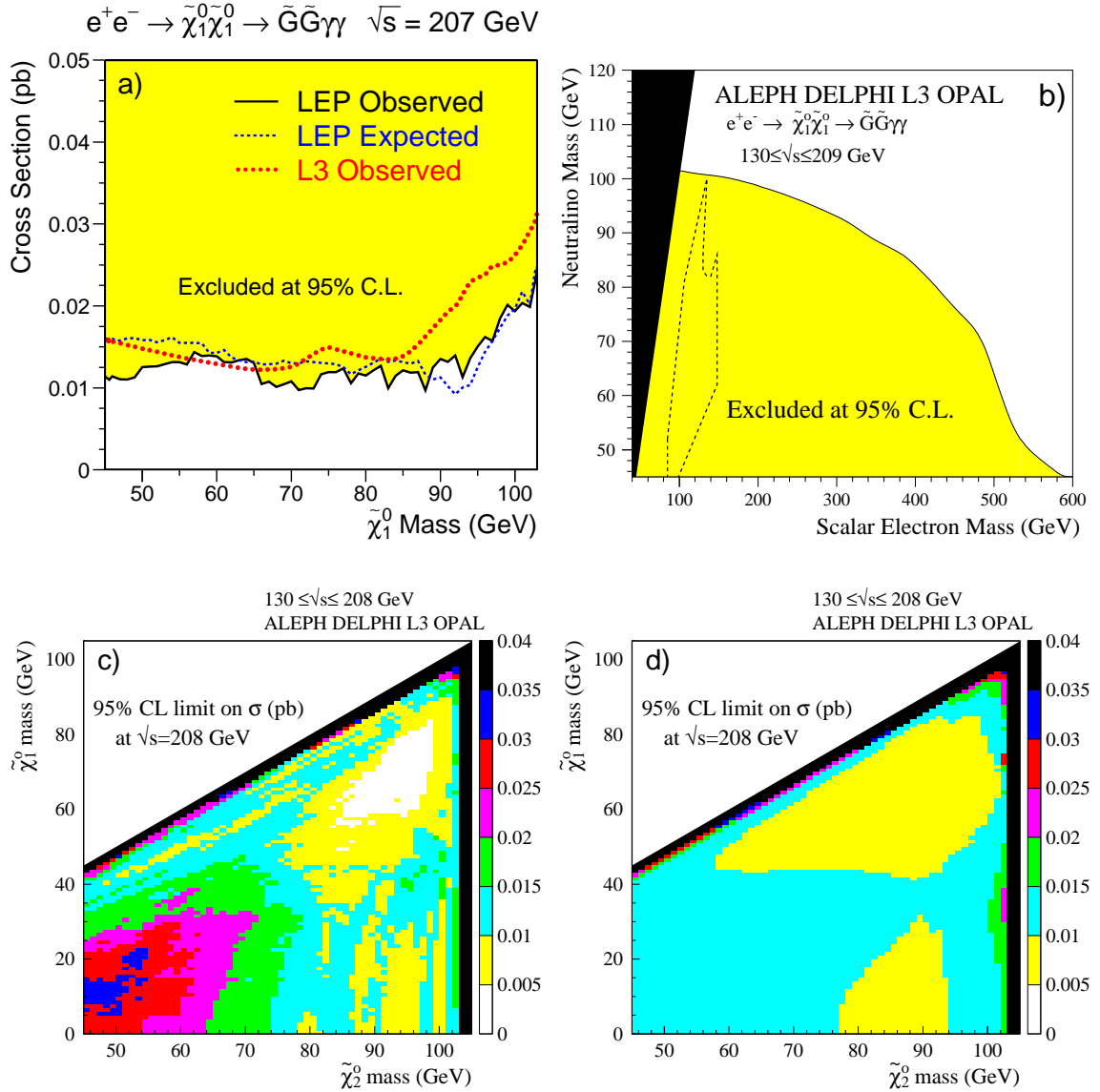
Figure E.4: **a)** Observed and expected upper limits on the production cross section of the reaction $e^+e^- \to \tilde{\chi}_1^0\tilde{\chi}_1^0 \to \tilde{G}\tilde{G}\gamma\gamma$, obtained from the LEP−combined search. The corresponding limits from my search are also shown. The limits were obtained at the 95% C.L. for $\sqrt{s} = 207$ GeV. Data collected at lower $\sqrt{s}$ were included assuming the signal cross section to scale according to the MGM model [194]. **b)** Region excluded for a pure bino neutralino model in the $(m_{\tilde{e}_R}, m_{\tilde{\chi}_1^0})$ mass plane. The region compatible with the GMSB interpretation of the CDF event [68] is also shown. **c)** Observed and **d)** expected cross section upper limits from the LEP−combined search for the process $e^+e^- \to \tilde{\chi}_2^0\tilde{\chi}_2^0 \to \tilde{\chi}_1^0\tilde{\chi}_1^0\gamma\gamma$. The limits were obtained at the 95% C.L. for $\sqrt{s} = 208$ GeV. The branching fraction for the $\tilde{\chi}_2^0 \to \tilde{\chi}_1^0\gamma$ decay was assumed to be 100%.

sensitive. The achieved improvement over the results of my analysis was equivalent to increasing the size of my data sample by about 50%. The region excluded at the 95% C.L. in the $(m_{\tilde{e}_R}, m_{\tilde{\chi}_1^0})$ mass plane is shown in Figure E.4b. The GMSB interpretation of the rare CDF event (Section 3.2.2) was ruled out by this combination of LEP analyses.

The LEP−combined search for the reaction $e^+e^- \to \tilde{\chi}_2^0 \tilde{\chi}_2^0 \to \tilde{\chi}_1^0 \tilde{\chi}_1^0 \gamma\gamma$ was also performed. The observed and expected limits are shown in Figures E.4c,d.

E.3   Searches for Extra Dimensions

All four LEP experiments have searched for the emission of Kaluza-Klein gravitons via the reaction $e^+e^- \to \gamma G$. As discussed in Section 3.3.1, this reaction leads to a single-photon with missing energy signature since the gravitons would escape undetected. Its differential cross section is expected to peak at low photon energies and polar angles (see Figure 3.16 p. 59).

n	M_D (TeV)			
	ALEPH [111]	DELPHI [216]	L3 [230]	OPAL [215]
2	1.26	1.31	1.50	1.09
3	0.95	1.02	1.14	0.86
4	0.77	0.82	0.91	0.71
5	0.65	0.67	0.76	0.61
6	0.57	0.58	0.65	0.53

Table E.2: Lower limits at the 95% confidence level on the new gravity scale M_D for different numbers of extra dimensions n, derived by the four LEP experiments from the individual searches for graviton-photon emission. The L3 search was described in Section 7.3. The OPAL limits were obtained using only the data set recorded in 1998 at $\sqrt{s} = 189$ GeV.

Searches performed by ALEPH [111], DELPHI [216], and L3 (Section 7.3) used the highest center-of-mass energy and luminosity LEP data sets collected during 1998-2000 at $\sqrt{s} = 189 - 208$ GeV, which corresponded to an integrated luminosity of
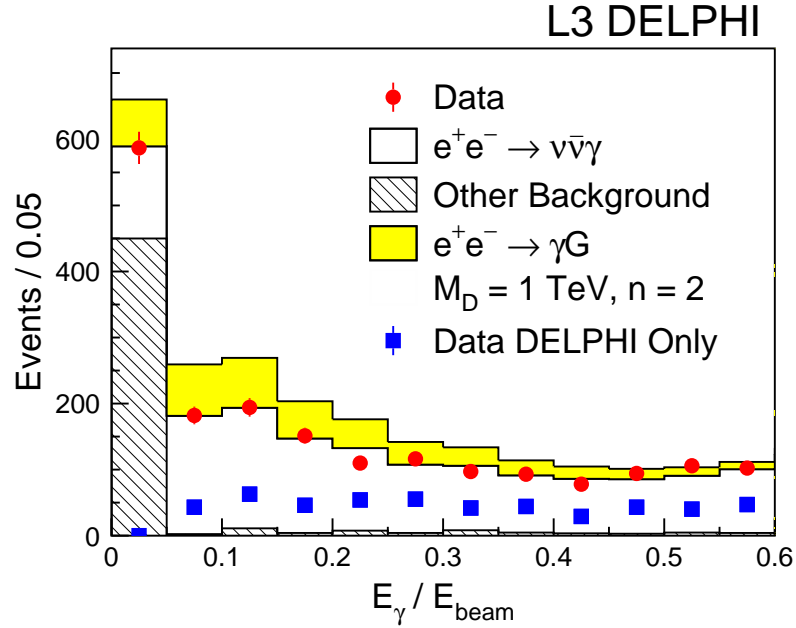
Figure E.5: Distribution of the ratio of the photon energy to the beam energy for the single-photon events selected by DELPHI and L3 together with the Standard Model prediction. Expected signal from the reaction $e^+e^- \rightarrow \gamma G$ is also shown for $M_D = 1$ TeV and $n = 2$. In addition, the individual contribution from DELPHI is shown as squares with error bars.

about 0.6 fb^{-1} per experiment. Since OPAL had analyzed only the data collected in 1998 at $\sqrt{s} = 189$, its results [215] were not considered for this combination.

Good agreement with the Standard Model prediction was observed by all experiments. In order to place limits on the new gravity scale M_D, each experiment performed a fit to its measured single-photon distributions under the assumption that the data contained a mixture of the signal and Standard Model background. The obtained limits are given in Table E.2.

The limits derived by my analysis are substantially tighter than those derived by DELPHI and ALEPH. This effect can be understood by examining Figure E.5, which shows the energy spectrum of the single-photon events selected by DELPHI and L3 together with the Standard Model prediction and the expected signal from the graviton-photon emission. This figure shows that in the region of highest sensitivity, $E_\gamma/E_{beam} < 0.2$, this sample was dominated by events from my single- and soft-photon selections (see Sections 6.3.8 and 6.5).
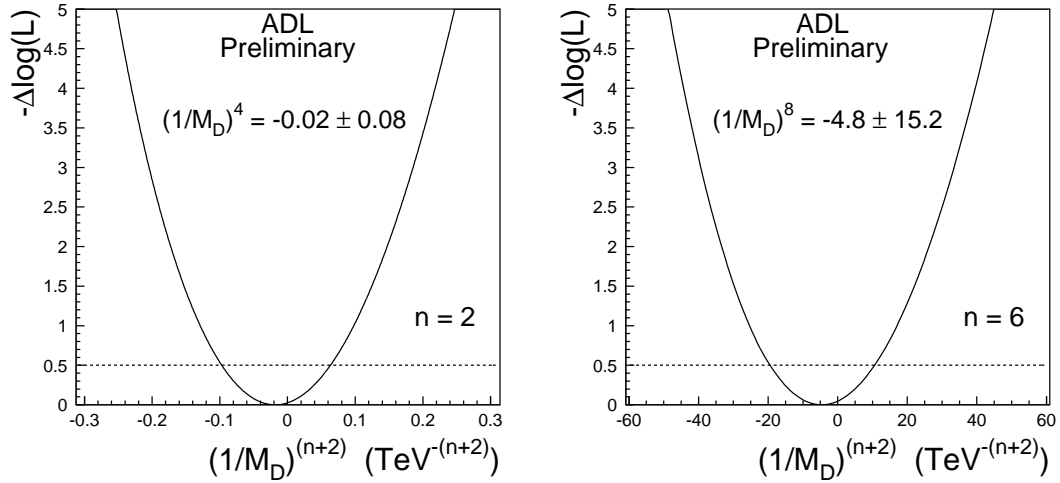
Figure E.6: The combined (ALEPH, DELPHI, and L3) negative log-likelihoods as functions of $(1/M_D)^{n+2}$ for $n = 2$ and $n = 6$. In each case, the minimum value was subtracted. The dashed line indicates $-\Delta \log \mathcal{L} = +0.5$.

Combination of the LEP Results

The combination was performed[4] using the likelihood functions derived by the ALEPH, DELPHI, and L3 individual analyses. Because the signal kinematic distributions were expected to change with the number of extra dimensions n, each experiment provided a separate log-likelihood function, $\log \mathcal{L}$, for each value of n. The systematic uncertainties were taken into account by each experiment separately. They were found to have no significant effect on the combined limits.

The individual $\log \mathcal{L}$ functions were added together, and the combined likelihoods were used to fit for the parameter $(1/M_D)^{n+2}$. This parameterization was chosen because, for a given n, the signal kinematic distributions were independent of M_D and the total cross section scaled as $(1/M_D)^{n+2}$. Figure E.6 shows that the combined $\log \mathcal{L}$ curves were close to parabolas.

The results of the fits are given in Table E.3, where the error on the parameter $(1/M_D)^{n+2}$ corresponds to a change in the negative log-likelihood with respect to its minimum of 0.5. The fitted values of $(1/M_D)^{n+2}$ were found to be in good agreement with the Standard Model expectation of zero.

---

[4]This work was done in collaboration with Dr. Stefan Ask (Lund University).

n	$(1/M_D)^{n+2}$		M_D (TeV)	R (mm)
2	-0.02 ± 0.08	TeV^{-4}	> 1.60	< 0.19
3	-0.09 ± 0.22	TeV^{-5}	> 1.20	$< 2.6 \times 10^{-6}$
4	-0.3 ± 0.8	TeV^{-6}	> 0.94	$< 1.1 \times 10^{-8}$
5	-0.9 ± 3.3	TeV^{-7}	> 0.77	$< 4.1 \times 10^{-10}$
6	-4.8 ± 15.2	TeV^{-8}	> 0.66	$< 4.6 \times 10^{-11}$

Table E.3: Fitted values of $(1/M_D)^{n+2}$ together with lower limits on the gravity scale (M_D) as functions of the number of extra dimensions (n). Upper limits on the size of the extra dimensions (R) are also given. All limits are LEP$-$combined (ADL) and are at the 95% confidence level.

Since no indication of a signal was found, limits on the new gravity scale were derived using the Bayesian likelihood method. At the 95% confidence level, a one-sided lower limits on M_D were obtained as

$$\mathrm{CL} = \frac{\int_0^{x_{95}} \mathcal{L}(x')dx'}{\int_0^{\infty} \mathcal{L}(x')dx'} = 0.95\,, \tag{E.1}$$

where $x = (1/M_D)^{n+2}$, $\mathcal{L}(x)$ is the combined likelihood function, and the integration is performed over the physical region $x > 0$. The derived limits are listed in Table E.3. The achieved improvement over the results of my analysis (Table E.2) roughly corresponds to increasing the size of my data sample by 50%.

The lower limits on the gravity scale can be converted into upper limits on the size of extra dimensions (R) using the following equation [80]:

$$G_N^{-1} = 8\pi R^n M_D^{n+2}\,, \tag{E.2}$$

where G_N^{-1} is Newton's constant of gravitation. Figure E.7 shows the radii of the extra dimensions as functions of the gravity scale M_D together with the obtained 95% C.L. upper limits on R. These limits are also listed in Table E.3.

The LEP$-$combined search for extra spatial dimensions excluded at the 95% C.L. gravity scales below between 1.6 TeV and 0.66 TeV for the number of extra dimensions
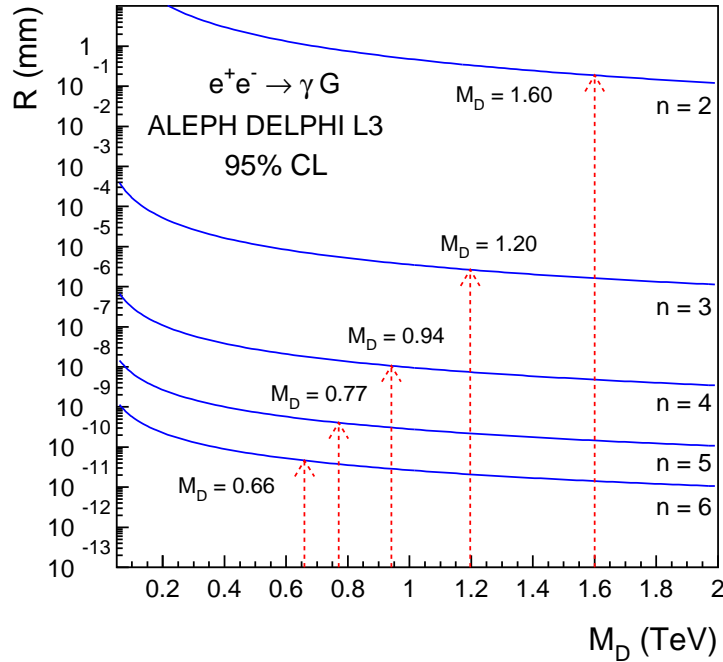
Figure E.7: The radii of the extra dimensions R as functions of the gravity scale M_D for $n = 2 - 6$. Arrows indicate the obtained upper limits on R.

between 2 and 6. The CDF and D∅ experiments at the Tevatron $p\bar{p}$ collider have searched for the production of Kaluza-Klein gravitons in monojet events. The current CDF result excludes gravity scales below 1.0, 0.77, and 0.71 TeV for $n = 2, 4$, and 6, respectively [223]. The D∅ experiment quoted slightly lower limits[5] [222]. Thus, for $n < 6$ the LEP limits are the best bounds to date on direct graviton emission in collider experiments. It should be noted that short-range tests of Newton's law [79] as well as astrophysical and cosmological constraints [78] provide similar or better bounds for the case of two extra dimensions. However, for $n > 2$ such bounds are relatively weak.

---

[5]The Tevatron results were obtained using the Run 1 data only. However, a preliminary analysis of the Run 2 data indicates that these limits will not be significantly improved at Run 2 [258].